

**Product Development Team
for
Advanced Weather Radar Techniques
Quarterly Report – 1st Quarter FY 06**

Nearly all tasks were represented at either 32nd Conference on Radar Meteorology/11th Conference on Mesoscale Processes, held in Albuquerque, NM, 22-29 October, 2005 or at the 17th Aviation, Range and Aerospace Meteorology Conference held 29 Jan. through 2 Feb. 2006 in Atlanta GA. Since these works constitute in-depth reports on specific activities, they are attached as appendices for their respective tasks.

NOTE: The first two tasks reported here are leftover from FY05. These tasks could not be completed in FY05 and so their completion is reported here.

05.6.16 GRIDS Radar Development (Re-tasked; effective April 21, 2005).

Formerly Tasks: 05.6.16 and 05.6.17 GRIDS development

This effort is aimed at wrapping up the GRIDS development effort. It includes finalizing the GRIDS technical report (to be published as a NOAA Technical Memorandum); interacting with the PDT's within the AWRP, to generate new tasking; analyzing data collected with the proto-GRIDS system and writing a scientific paper; and (at no cost to FAA) finishing the ETL-based GRIDS web pages which will serve existing data and images and publications.

Tasks 05.6.16.01 (GRIDS Tech. Report) and 05.6.16.02 (Data Analysis and Publication) were scheduled to be completed in Q1 of FY06.

a) Current Efforts

See Appendix 1

b) Planned Efforts

None; task is complete.

c) Problems/Issues

None

d) Interface with other Organizations

None.

e) Activity Schedule Changes

Tasks 05.6.16.01 (GRIDS Tech. Report) and 05.6.16.02 (Data Analysis and Publication) will be completed in Q1 of FY06.

05.6.27 Polarimetric Freezing Rain/Drizzle

Winter weather and in-flight icing products are both concerned with freezing rain and freezing drizzle. Both phenomena represent serious safety challenges for aircraft on the ground as well as in flight. The ability to reliably detect areas of freezing precipitation is unavailable with current radars.

a) Current Efforts

05.6.27.3 Is complete. A report on the results was presented at the 2006 ARAM, and is attached as Appendix 2.

b) Planned Efforts

None; task is complete.

c) Problems/Issues

None

d) Interface with other Organizations

None.

e) Scheduled Activity Changes

None.

06.6.19 Common Radar Data Acquisition Techniques for FAA Radars (WSR-88D, TDWR, ASR-9)

Traditionally, algorithm techniques are developed for the radar product generator. This approach limits the algorithms to utilize data after its collection at the radar. Developing techniques for use on the data collected at its origin and in its native forms allows for new approaches to address FAA needs across multiple radar platforms.

a) Current Efforts

No progress to report.

b) Planned Efforts

None.

c) Problems/Issues

None.

d) Interface with other Organizations

None.

e) Activity Schedule Changes

None.

06.6.22 Polarimetric Mixed-Phase Cloud Identification

Polarimetric radar measurements are sensitive to hydrometeor types and mixed-phase precipitation in particular. The measurements have potential for icing detection and for determining regions within storms in which hazardous icing conditions are likely to exist. The measurements may also have benefits for designating regions within storms where the probability of icing is low.

a) Current Efforts

NCAR and NSSL

See Appendices 3, and 4.

b) Planned Efforts

Continue with scheduled work plan.

c) Problems/Issues

None.

d) Interface with other Organizations

None.

e) Activity Schedule Changes

None.

05.6.25 Polarimetric Freezing Level Detection.

An ability to detect the freezing level within clouds and precipitation is important for establishing in-flight icing hazards and for winter-weather products such as rain-snow discrimination. Designated freezing levels may also prove useful for more accurate numerical model initialization and thereby improve forecasts of hazardous weather. A fast-track non-polarimetric version of the freezing-level detection algorithm could be implemented in just a few years which may improve products like the Current Icing Potential (CIP) algorithm without having to wait for dual-polarization upgrade to the WSR-88D.

a) Current Efforts

See Appendix 5.

b) Planned Efforts

Continue with scheduled work plan.

c) Problems/Issues

None.

d) Interface with other Organizations

None.

e) Activity Schedule Changes

None.

05.6.26 Polarimetric winter quantitative precipitation estimation.

Winter quantitative precipitation estimation (QPE) is important to winter weather algorithms and ground de-icing operations. Current systems adjust radar-based winter QPE using measurements from in situ sensors such as gauges. A capability to retrieve particle size distributions and to discriminate among various hydrometeor types with polarimetric radar should lead to better predictions of winter storm precipitation intensity and, consequently, to more efficient ground de-icing activities, enhanced flight safety, and increased airport capacity.

a) Current Efforts

See Appendix 6.

b) Planned Efforts

Continue with scheduled work plan.

c) Problems/Issues

None.

d) Interface with other Organizations

None.

e) Activity Schedule Changes

None.

05.6.29 NCAR NTDA Implementation in NEXRAD OpenRPG/CODE. (NCAR).

Collaboration with the Turbulence PDT for the WSR-88D ORPG implementation of the NCAR Turbulence Detection Algorithm (NTDA) is a task that allows AWRT to collaborate with this PDT in their goal of having a national, 3-D turbulence product for aviation users. The Turbulence PDT has developed the turbulence algorithm. The AWRT PDT will collaborate with the Turbulence PDT in the implementation of NTDA within the WSR-88D environment. This assistance includes hardware purchases, software acquisition of the ORPG CODE and software engineering assistance.

a) Current Efforts

The initial version of the NTDA has been implemented in OpenRPG/CODE. Special efforts were made to make the code readable and to thoroughly document it. The implementation was verified by quantitatively comparing the output EDR and confidence, as well as numerous intermediate fields, to output from the TRS real-time demonstration application. Agreement between the two incarnations are perfect for higher elevation angles. On the low-elevation split cut tilts, occasional minor discrepancies appear to be due to the different algorithms used to combine the surveillance and Doppler moment sweeps in the two environments and are not a concern.

Implementation of the NTDA Final Product application, which writes the NTDA output to the RPG Product Database, was completed.

CODE's Code View Graphics (CVG) utility was configured to display the NTDA Final Products. The CVG graphics were verified to be qualitatively identical to MATLAB plots of the NTDA output.

With guidance from Betty Bennett and Dave Smalley of MIT Lincoln Laboratories, the capability to run the OpenRPG/CODE on real-time LDM data has been set up.

A PowerPoint presentation depicting the AND's implementation design has been created and reviewed internally.

b) Planned Efforts

Working with the Turbulence PDT task 06.7.3.1.1, continue to enhance the NTDA and tune its parameters.

Develop the capability to profile the NTDA CODE implementation in order to assess resource requirements and identify opportunities for optimization.

Continue to run the NTDA on real-time LDM data to verify the CODE implementation's stability.

Perform an NTDA code review with senior software engineers at NCAR/RAL.

Continue pursuing the NTDA approval process.

c) Problems/Issues

None.

d) Interface with other Organizations

NWS Office of Science and Technology, MitreTek Systems, BAE Systems.

e) Scheduled Activity Changes

None.

05.6.34 High-Resolution National 3-D Radar Mosaic

The area for which any arbitrary ARTCC or AFSS has responsibility encompass the coverage area of several WSR-88D installations. Numerical models have reached such a level of sophistication that they now use radar data to initialize model runs. There are no existing products that use data from more than one radar, and no gridded products that use the full 3D characteristics of these data. The real-time CONUS 3D mosaic system will be stabilized and enhanced in FY 2005 based on the findings during FY 2004. The AWRT can also provide customized products as requested by other AWRP PDTs. For example, a suite of 2-D products will include VIL (vertically integrated liquid), hail products, and layer composite reflectivities will be derived from the 3D mosaic. This task supports several other PDTs by providing them with full 3D grids and derived 2D grids that take advantage of 3D and 4D information.

a) Current Efforts

See Appendix 7.

b) Planned Efforts

Continued study of quality control, VPR and gap-filling in the 3D mosaic and time synchronization of multiple radar observations.

c) Problems/Issues

None.

d) Interface with other Organizations

Regenerated and provided 3-D mosaic data sets based on a request from the NCAR icing PDT.

Discussions with the NCAR icing PDT on the possibility of creating an un-QC'd national 3D mosaics for supporting aviation icing products development.

e) Scheduled Activity Changes

None.

05.6.35 Adaptive Radar Mosaic System

This task addresses the availability high-resolution reflectivity data that increases the reflectivity data resolution by reducing the range spacing of reflectivity samples from 1 km to 250 m. This task will develop and evaluate techniques for mapping these new data in the most computationally efficient manner so as to minimize and data latency.

a) Current Efforts

See Appendix 8.

b) Planned Efforts

Continued development of single radar Cartesian grid (e.g., synchronization and gap-filling components) will continue. A new CONUS 3-D mosaic based on the SRC grids will be implemented.

c) Problems/Issues

None.

d) Interface with other Organizations

None.

e) Activity Schedule Changes

None.

A ground-based remote icing detection system (GRIDS) perspective on the November 11, 2003 SLD case during AIRS2

Timothy Schneider & Carroll Campbell
NOAA Earth System Research Laboratory

Abstract

On 11 November 2003, the Ground-based Remote Icing Detection System (GRIDS), captured a marked transition in cloud composition that moved across the AIRS II field program suite of instruments, based at Montreal's Mirabel Airport. Glaciated clouds, which presented little, if any icing threat, gave way to warm-topped, stably-stratified, water dominated cloud at subfreezing temperatures. As documented by in-situ aircraft sampling, these clouds featured significant water contents and supercooled large drops (SLD) with diameters exceeding 300 microns, resulting in moderate and even moderate-to-severe icing conditions. Most telling of the transition from the GRIDS' perspective, was a significant change in the depolarization ratio, from that indicative of ice to that of liquid droplets. [Presented at AMS-ARAM, January, 2006; Atlanta, GA.]

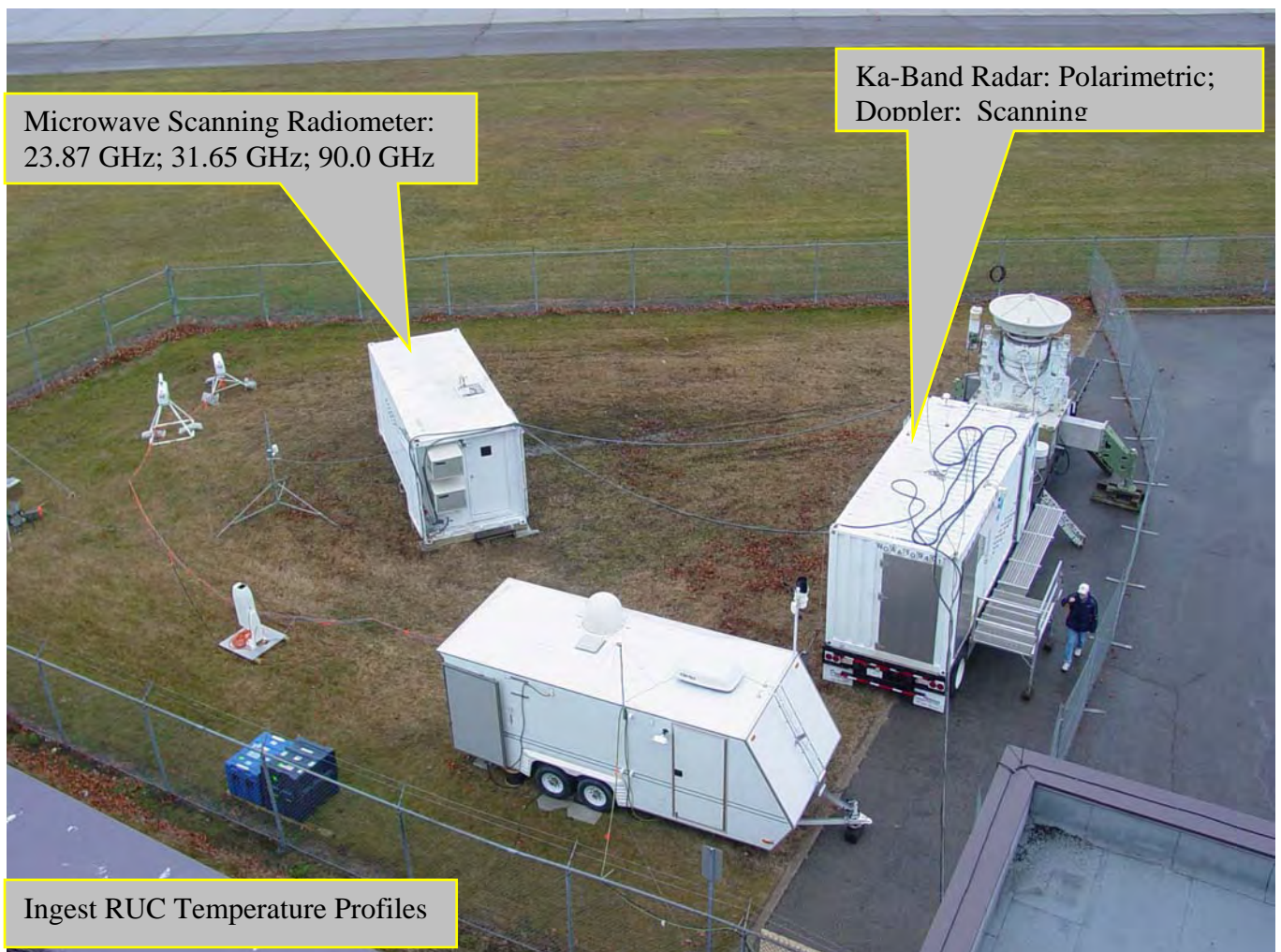


Figure 1 GRIDS layout at the "Teksol" site. The NASA NIRSS system is adjacent to GRIDS. (Photo courtesy of Andrew Reehorst, NASA)

Figure 1 illustrates the layout of the GRIDS system at the AIRS2 “Teksol” site at Mirabel Airport in Quebec, Canada. Fig. 1 also indicates the primary components of hardware that comprise GRIDS. Critical measurements include the radar reflectivity, the radar depolarization ratio, the integrated cloud liquid water from the microwave radiometer, and the ingested NOAA-NCEP Rapid Update Cycle model data for temperature profiles.

Figure 2 shows the output of the GRIDS icing algorithm, which is described in Figure 3.

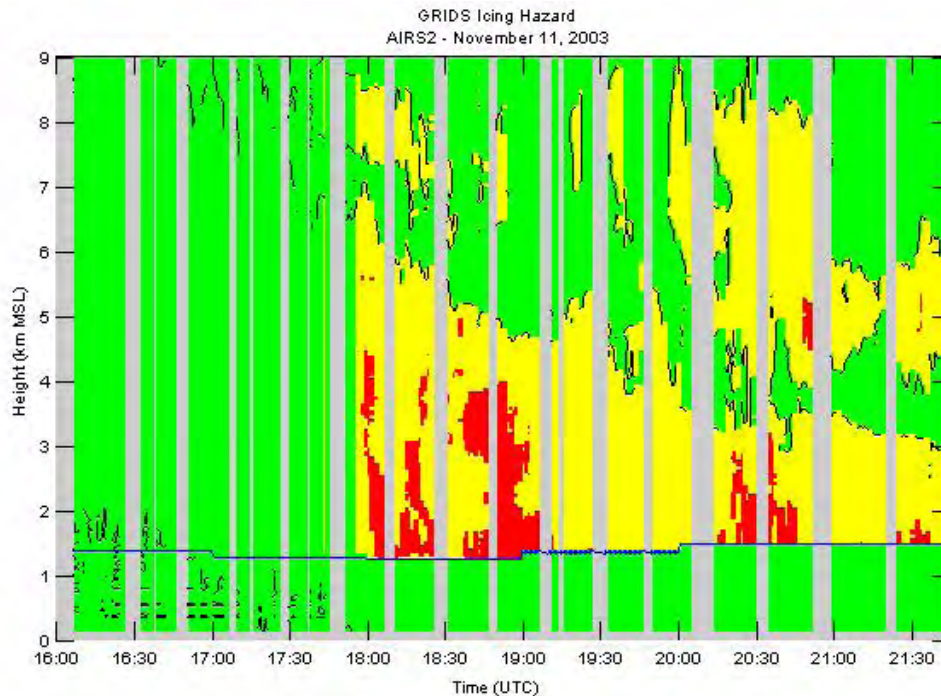


Figure 2 The end result: the GRIDS icing hazard product. See text for explanation.

As presented in Figure 2 (and Fig. 3) in the GRIDS icing hazard product, **green** represents no hazard; **yellow** indicates the potential presence of a hazard (one or more criteria suggests a hazard, but the threat is not definitive); and **red** indicates a definitive hazard. The thin **blue** line is the freezing level inferred from RUC temperature profiles.

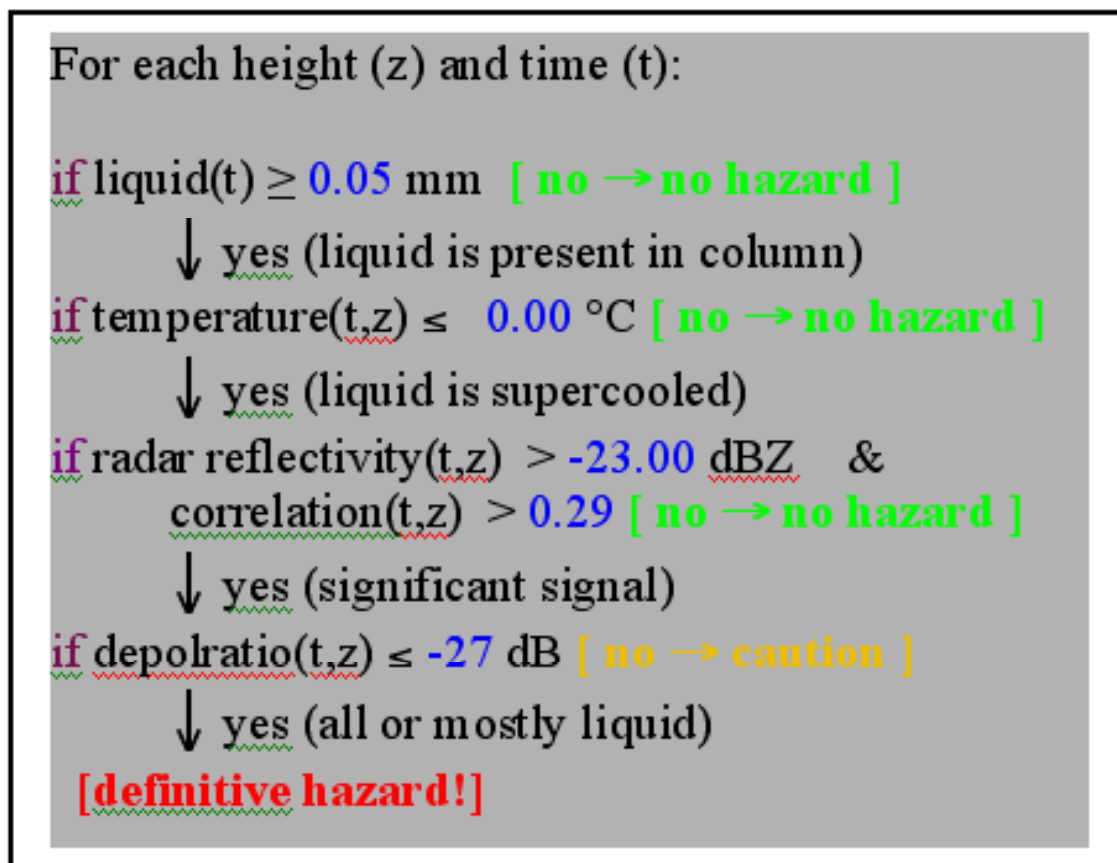


Figure 3 A simple decision tree representation of the GRIDS icing algorithm.

At present the GRIDS algorithm represents a simple decision tree: only the presence or potential presence of a threat is indicated, not the severity of a threat. In a qualitative sense, the GRIDS icing algorithm did well in indicating icing (red) as confirmed by in situ observations: where the aircraft encountered icing in the Mirabel region, GRIDS indicated icing (e.g. at ~20:00 UTC). The broad areas of yellow suggest that there is some over-prediction, this remains to be quantified rigorously from the AIRS2 in situ aircraft data.

Figures 2 (RUC temperature), 4 (cloud liquid) and 6 (radar reflectivity and depolarization ratio) present the data from GRIDS used in the icing algorithm shown in Figure2.

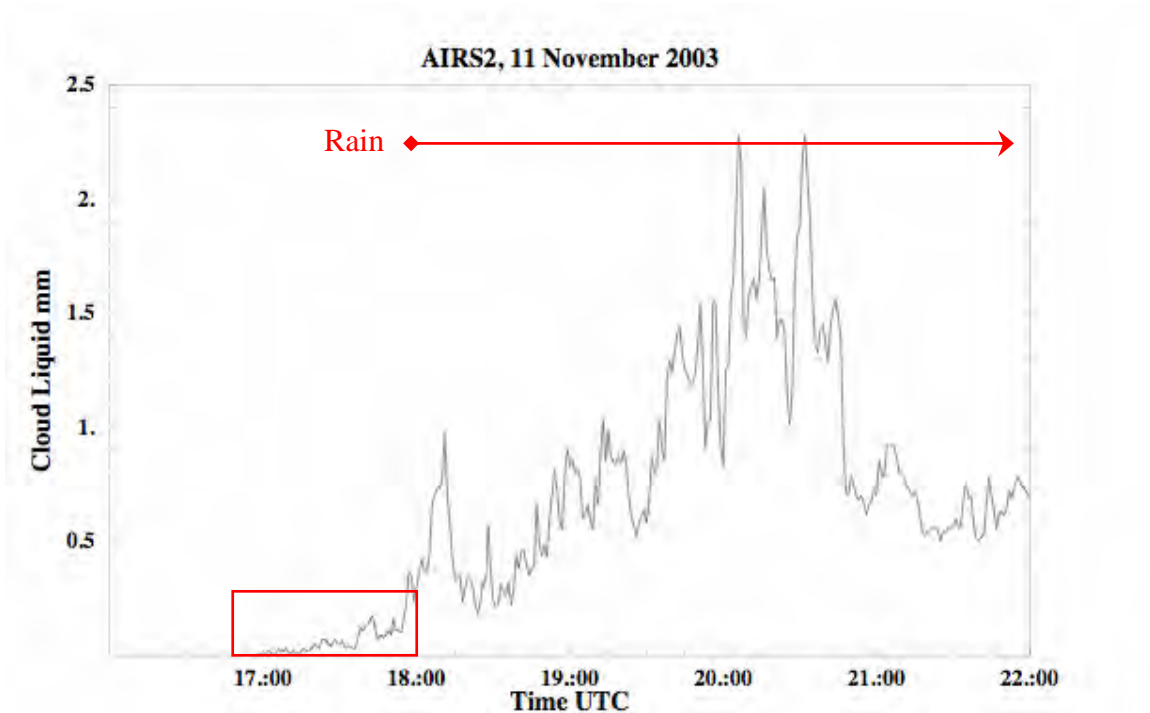


Figure 4 Microwave radiometer, derived integrated cloud liquid water. When rain is present the absolute value of the cloud liquid is suspect, although the presence of liquid is not.

Radiometer data collected during the period of time indicated by the red box in Fig. 4 were used to retrieve the mean cloud temperature. The technique depends on the differences in the temperature dependence of the 30 GHz and 90 GHz. The results of this technique are shown in Figure 5. Because of the manner in which NASA operated its radiometers, there were not a large number of data points for this estimation, and so the results are statistically suspect. The result is included to indicate the nature of the technique, and to call attention to it. Statistically significant results from other cases compared favorably with in situ results.

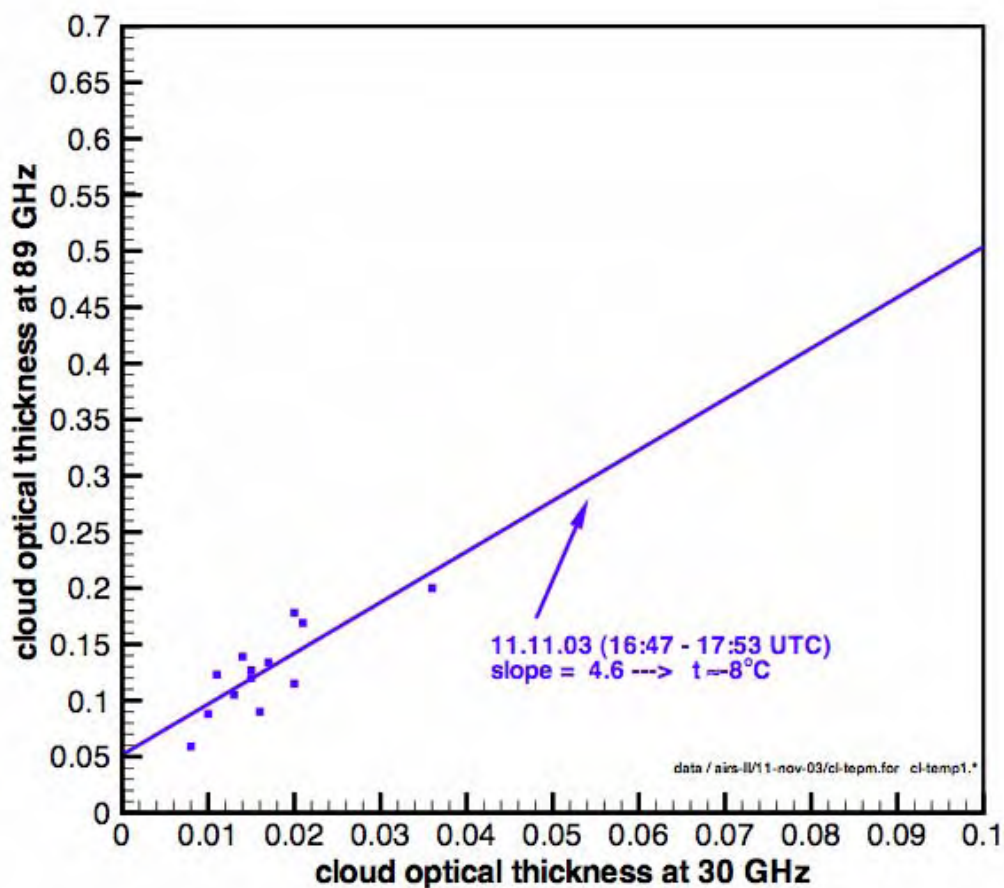


Figure 5 Retrieval of the mean cloud liquid temperature using the 30 GHz and 90 GHz radiometer channels. (Data courtesy of Andrew Reehorst, NASA).

The production of SLD just after 20:00 UTC is clearly indicated in the depolarization ratio (bottom panel, Fig. 6). The black boxes in Fig. 6 indicate the period where the NASA Twin Otter made a spiral decent and missed-approach over Mirabel and the GRIDS radar was placed in the vertically pointing spectra mode.

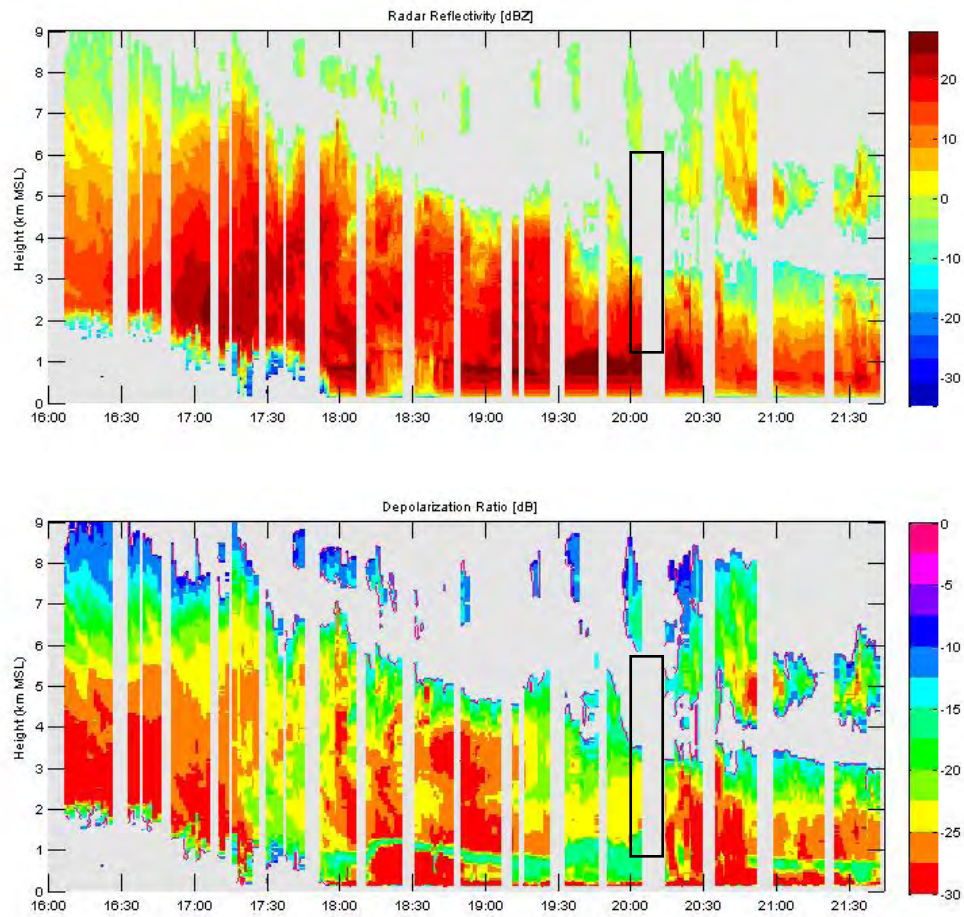


Figure 6 Time-height (40°) images of the radar reflectivity (top) and depolarization ratio (bottom).

Vertically point Doppler spectra are useful for separating ice and liquid in profile. The Doppler velocity and spectral width at 2.5 to 3.5 km AGL are indicative of the formation of liquid. Individual Doppler spectra (not shown; presented elsewhere) support this interpretation.

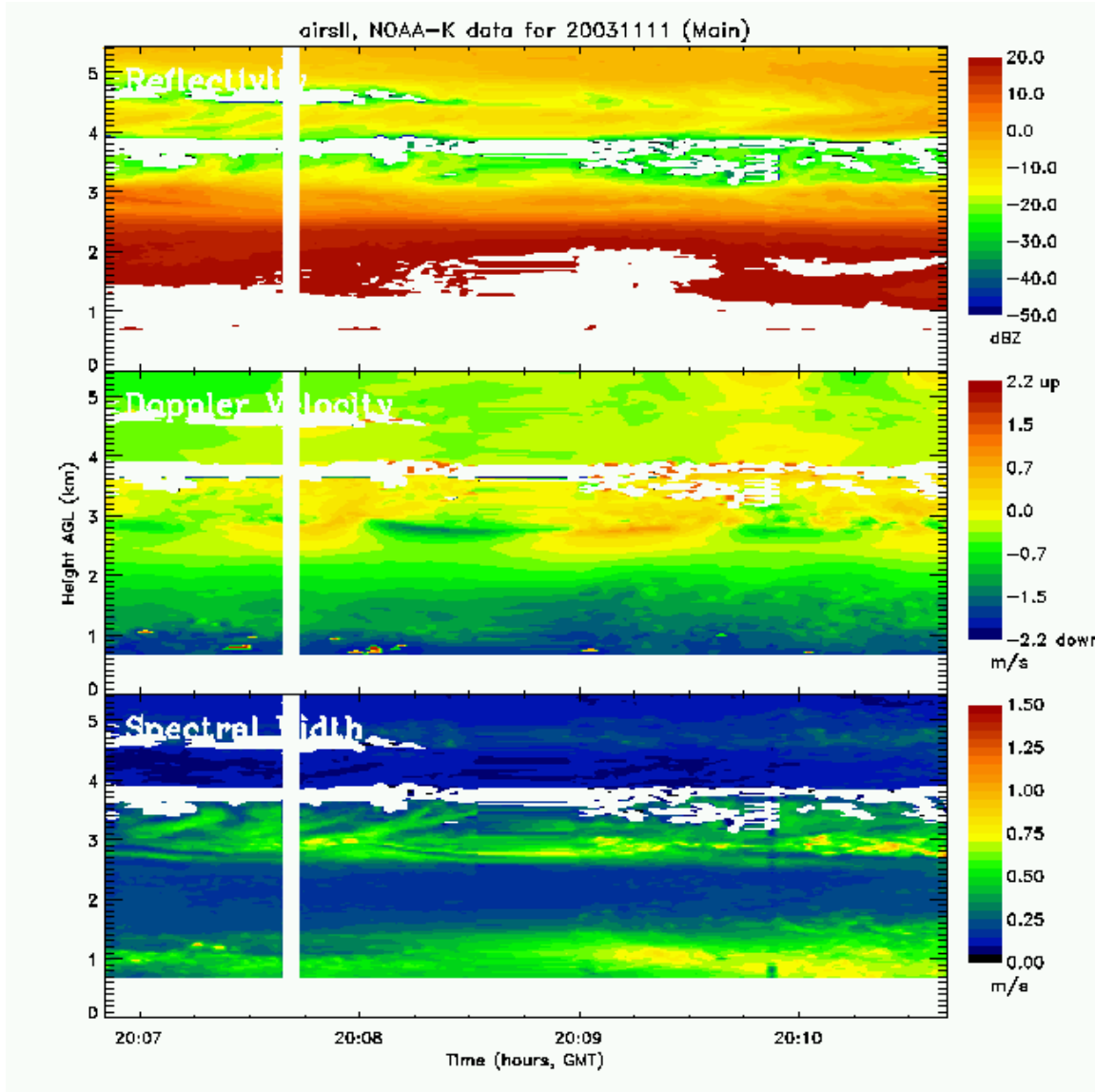


Figure 7 Vertically pointing Doppler moments: reflectivity (top); Doppler velocity (middle); spectral width (bottom).

Conclusions:

- GRIDS provided high resolution, detailed information of cloud-physical properties (microphysical properties can be inferred)
- More can be done with the scanning (RHI) data and; vertical Döppler spectra & radiometer data for this case.
- We are gaining confidence in the GRIDS concept and algorithm
- We need to statistically characterize the icing detection performance
- The real utility is in assimilation, parameterization and verification, and this should be demonstrated.

Task 05.6.27.3

Optimization of Hydrometeor Classification Using Multivariate Statistical Techniques

1. Introduction

The upcoming polarimetric upgrade of WSR-88D radars provides the opportunity for unprecedented improvement in the classification of hydrometeors. For the aviation industry, this polarimetric upgrade promises to improve classification of the spectrum of hydrometeors that affect operations (e.g., ice, snow, hail, and rain). To identify these hydrometeors, several researchers have implemented fuzzy-logic algorithms. Although the fuzzy-logic approach has shown success in the discrimination of rain and hail, an important consideration is whether a multivariate statistical technique may outperform fuzzy-logic methods. The purpose of this research is to investigate multivariate statistical relationships among polarimetric variables that may improve the classification of hydrometeors of interest to the aviation industry. This report describes the data, methodology, and crossvalidation results for hail and rain classes.

2. Data and Methodology

Hail and rain classes are investigated first owing to the large amount of ground truth data available. To date, the training data set includes 106 hail reports and 153 rainfall reports located within 10–100 km of the National Severe Storms Laboratory's KOUN prototype dualpolarization radar (KOUN). The 106 hail reports are associated with 17-hail producing events during 2003 and 2004 and sources of these reports are Storm Data and the Joint Polarization Experiment (JPOLE). Hail reports are validated by comparing their location to near-by storm structure characteristics within a -15 to 5 min time-window. The 153 rainfall reports are associated with two MCSs without hail reports in Storm Data during June 2004 and the source of these reports is five-min rainfall data from 25 stations within the Oklahoma Mesonet. Although these data are sufficient for this preliminary study, the dataset will be expanded to increase the sample size.

Four polarimetric variables: Z_H , Z_{DR} , K_{DP} , and ρ_{HV} comprise the polarimetric dataset. These variables are attained by a two-part process. First, we identify the range gate closest in time and space to each hail report and rainfall report. Second, we retain polarimetric variables located within $\pm 1^\circ$ azimuth and ± 0.75 km of the closest range gate. This kernel-approach takes into consideration the uncertainty inherent in hail report locations and is used to explore which part of the data distribution produces the best statistical results. These polarimetric data kernels and the hydrometeor class (hail or rain) are the input for the two multivariate statistical techniques investigated: quadratic and canonical discriminant analysis.

3. Results of Quadratic and Canonical Discriminant Analysis

Quadratic and canonical discriminant analysis methods applied to kernel data values (including quartiles and the average) reveal that using the 95th percentile polarimetric variables produces the best results. Best results are measured by a set of accuracy and skill measures, including hit rate (HR), probability of detection (POD), probability of false detection (POFD), false alarm rate (FAR), critical success index (CSI), bias, Pearce skill score (PSS), and Heidke skill score (HSS). The statistical significance of scores for both the quadratic and canonical approaches is assessed by bootstrap crossvalidation (Fig. 1). The distribution of accuracy measures and skill scores indicates that both discriminant functions are very promising approaches to hydrometeor classification.

4. Future Work

This preliminary investigation indicates strongly that multivariate statistical techniques are a promising approach to polarimetric hydrometeor classification. These positive results are the catalyst for further work, including increasing our hail and rain sample sizes and adding new classes, such as ground clutter, biological scatters, and mixed phase precipitation, to the training dataset.

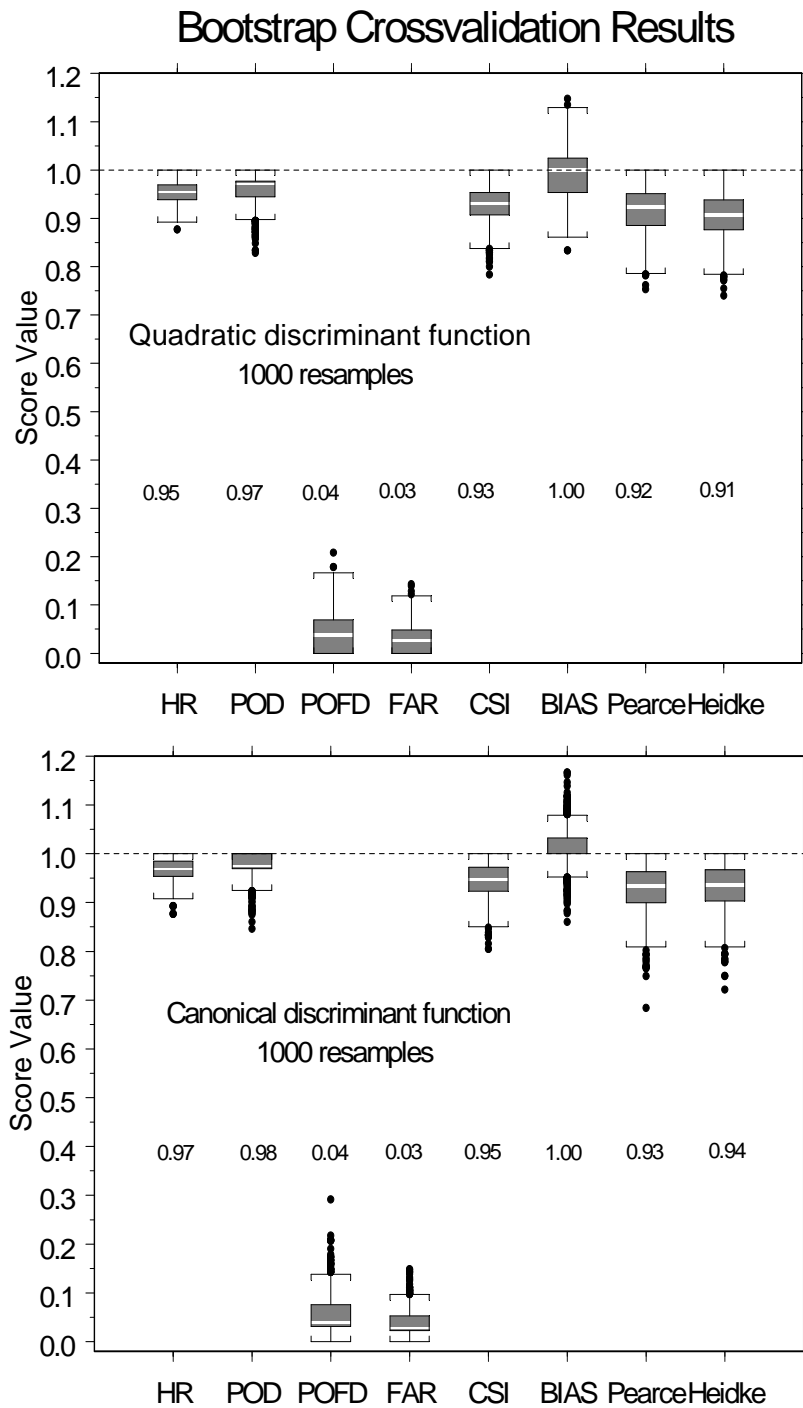


Figure 1. Box and whisker plots of bootstrap crossvalidation results for quadratic and canonical discriminant functions. Typed scores show the median value for each accuracy measure and skill score. The box indicates the interquartile range whereas the whiskers indicate values within 1.6 x interquartile range.

OBSERVATIONS OF WINTER STORMS WITH 2-D VIDEO DISDROMETER AND POLARIMETRIC RADAR

Kyoko Ikeda¹, Edward A. Brandes¹, Guifu Zhang², and Steven A. Rutledge³¹National Center for Atmospheric Research, Boulder, Colorado²University of Oklahoma, Norman, Oklahoma³Colorado State University, Fort Collins, Colorado

1. Introduction

The Winter Icing and Storms Project 2004 (WISP04) was conducted from February to April 2004 in north central Colorado. Program objectives were to evaluate remote sensing techniques for icing detection and for quantifying winter precipitation in support of airport deicing operations. Measurements from a S-band dual-polarization radar and a two-dimensional video disdrometer are being used to develop radar-based algorithms to discriminate between rain and snow, quantify winter precipitation, and improve parameterization of winter precipitation in numerical forecast models. An ability to match radar-measured and disdrometer-based radar parameters is essential when developing algorithms for winter precipitation. Video disdrometers provide important information regarding hydrometeor size, shape, terminal velocity, and number concentration at high temporal resolution. As a first step in this project, we verify that the radar detects subtle changes in the character of winter precipitation.

Here radar reflectivity factor (reflectivity or Z_H , hereafter) and differential reflectivity (Z_{DR}) are calculated from disdrometer data collected on 5 March 2004, an event in which precipitation changed from rain to snow. The calculations are based on scattering amplitudes of raindrops and snow computed with the T-matrix method. The scattering matrix during the transition and snow phases was allowed to vary according to an empirical relation between particle size and bulk snow density developed from disdrometer observations. Reflectivity and differential reflectivity calculations based on disdrometer observations show good agreement with the radar measurements. The radar measurements of Z_H and Z_{DR} are then used to retrieve snow particle size distributions for comparison with the disdrometer observations. A case study from a precipitation event on 20 February 2004 will be also presented at the conference.

The dataset and a brief description of the disdrometer are given in section 2. Section 3 discusses the disdrometer calculations for reflectivity and

differential reflectivity followed by a comparison of the estimates with the radar measurements in Section 4. Results from retrievals of particle size distributions are presented in section 5. A summary and concluding remarks are given in section 6.

2. Data

The radar data were collected with NCAR's S-band dual-polarization radar located at Marshall, Colorado. Scan strategies included sector scans at 0.5 and 1.5° antenna elevation and range-height indicator (RHI) scans over a 2-D video disdrometer placed at a range of 19 km and an azimuth angle of 42° from the radar.

The disdrometer consists of two line-scan cameras providing front and side views of hydrometeors falling into the instrument. Each camera has a single line of 700 photo-detectors positioned opposite a light source. Hydrometeors falling through the 10 cm by 10 cm measuring area block the light source, shadowing some photo-detectors at a horizontal resolution of 0.15 mm. The number of blocked photo-detectors is recorded for each camera at a frequency of 51.2 kHz. Vertical resolution typically varies between 0.03 mm and 0.1 mm depending on particle fall speed. The sampling creates image projection slices of the hydrometeors.

Information provided on individual hydrometeors includes silhouette images, height and width information from each camera, and the particle terminal velocity. Particle terminal velocity is computed from the vertical distance between the two camera planes and the time the hydrometeor takes to break each plane. Raindrop axis ratio, canting angle, and horizontal velocity can also be obtained with the instrument. The disdrometer is equipped with temperature and wind sensors. A detailed description is found in Kruger and Krajewski (2002). Field notes from a crystal observer supplement the disdrometer data. Observations of crystal type, size, degree of riming, and amount of aggregation were made every 15 minutes.

3. Modeling considerations

Radar reflectivity (in $\text{mm}^6 \text{m}^{-3}$) at horizontal (H) and vertical (V) polarization can be computed from

$$Z_{H,V} = \frac{4\lambda^4}{\pi^4 |K_w|^2} \sum_{i=1}^M N(D_i) |f_{H,V}|^2 \Delta D \quad (1)$$

* Corresponding author address: Kyoko Ikeda, National Center for Atmospheric Research, P.O. Box 3000, Boulder, CO 80307
E-mail: kyoko@ncar.ucar.edu

where λ is the radar wavelength, K_w is the dielectric factor of water, $N(D_i)$ is the size distribution for the i th size category having an equivalent diameter (mm) between D_i and $D_i + \Delta D$, M is the total number of size categories, and $|f_{h,v}|$ is the backscattering amplitude at horizontal and vertical polarization (see Zhang et al. 2001). Reflectivity is expressed in dBZ ($10 \times \log_{10} Z_H$). In this study, the disdrometer data were quantized into size categories of 0.2 mm over the range of 0.1–20.1 mm for snow and 0.1–8.1 mm for rain.

The differential reflectivity (Z_{DR} in dB) is defined as

$$Z_{DR} = 10 \times \log_{10} (Z_H / Z_V). \quad (2)$$

Z_{DR} is sensitive to particle bulk density, shape, and canting angle and can be interpreted as the reflectivity-weighted mean axis ratio of the illuminated hydrometeors. The Z_{DR} values were corrected for system bias (−0.08 dB). The bias was determined from radar data that was collected by rotating the antenna while pointing vertically in light rain. In theory, raindrops should produce a Z_{DR} value of 0 dB in the mean when viewed from below.

The scattering amplitude is computed with the T-matrix method (Barber and Yeh 1975). Input parameters include the dielectric constant, particle shape (e.g., axis ratio), and the temperature. For rain these parameters follow Zhang et al. (2001).

Properties of snow are complex. Aspect ratios and bulk densities continuously change throughout storm evolution making computations of the scattering

amplitudes less straight forward. In this study, the particles were assumed to be oblate spheroids having a fixed axis ratio (vertical divided by horizontal) of 0.7 and with their major axis along the horizontal.

The effective dielectric constant (Ishimaru 1991) was derived from an empirical relationship between snow bulk density and particle size based on disdrometer data collected at Marshall during winter seasons (Fig. 1). Snow bulk density was computed using 5-minute measurements of precipitation volume from the disdrometer and mass from onsite precipitation gauges. All instruments were located inside wind shields. Data points in Fig. 1 were from PSDs with total particle counts greater than 1000. Wind speeds were less than 2 m s^{-1} . The power-law relation between snow bulk density and median equivolumetric diameter is fitted through the data points (red line, Fig. 1). The dataset contains both rimed and unrimed snow. Nevertheless, the data closely follow the inverse relation between size and density found by Holroyd (1971) from ground-based observations of unrimed snowflakes. For this study, we use an effective dielectric constant based on the power-law relation derived from our disdrometer data. By using this relationship, the scattering amplitude allows for a variation in snow bulk density that is anticipated to occur with storm evolution. This approach is similar to that taken by Ryzhkov et al. (1998) who proposed a method to compute cloud ice water content using a relation between particle bulk density and radar cross sections or effective ice crystal diameter.

4. Observations: 5 March 2004

Precipitation on 5 March 2004 was dominated by an intense 500 mb trough across the western United States and an associated surface low pressure system over central Oklahoma. Low-level winds from the north and east-northeast behind the low pressure center created a favorable condition for upslope stratiform precipitation in the WISP04 domain. Above the upslope airmass (>5 km MSL), winds were mostly westerly or southwesterly, and the atmosphere was cloud-free. An abrupt decrease in surface temperature from 5.5°C to 0.5°C occurred over a 15-minute period at approximately 0100 UTC. The surface temperature changed only slightly afterward remaining between 0.5 and -0.5°C . The temperature at cloud top (4–5 km MSL) was generally between -13 and -18°C .

a. Precipitation

Most of the precipitation fell between 0000 and 0500 UTC. Table 1 summarizes the hydrometeor types noted by the crystal observer. Early precipitation was light rain (Period A). The surface layer moistened and cooled rapidly as the rain rate increased. A rain-to-snow transition (Period B) occurred with the temperature decrease at 0100 UTC. The field notes indicate ice pellets were mixed with raindrops. The smaller terminal velocities of ice pellets, compared with raindrops, are clearly depicted in the disdrometer data (Fig. 2). [Empirical relationships from previous

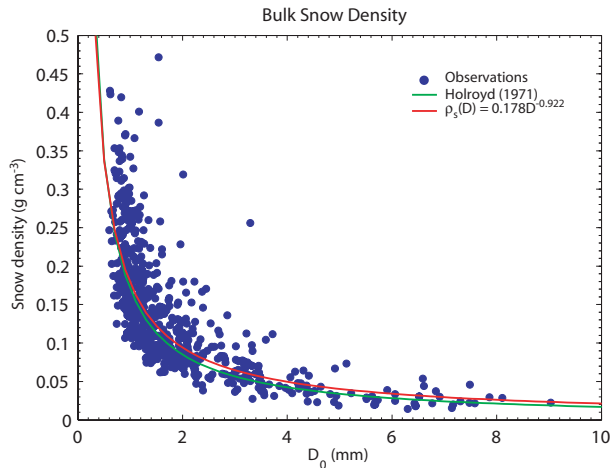


Figure 1: Relation between bulk snow density (ρ_s) and median equivolumetric diameter (D_0). Data points are from snow observations between February 2003 and April 2005. Each point represents an average quantity over a 5-minute interval. The red line is a power-law fit through the data points. An inverse relation ($\rho_s = 0.170D^{-1}$) for unrimed snow aggregates from Holroyd (1971) is also shown.

investigators are overlaid for reference.] A small number of large aggregates also existed at this time which caused an increase in the particle median volume diameter to 4.6 mm (Fig. 3). The mixed-phase precipitation period ended by 0120 UTC.

Later (0120-0145 UTC; Period C), observed precipitation consisted mostly of ice pellets and some small aggregates. Beginning at 0145 UTC (Period D), 1-3 mm plate-like crystals (plates and dendrites) became noticeable, and the number of large aggregates increased significantly. (Figs. 2 and 3, Period D).

Another change in precipitation occurred at approximately 0220 UTC. Small lump graupel and irregularly shaped snow pellets were mostly observed (Period E). The field notes indicate much less aggregation at this time. The terminal velocity appears to have a slightly stronger size-dependency compared with the previous stage (Fig. 2, Periods D and E). The median volume diameter decreased significantly between the period of heavy aggregation (Period D, $D_0 = 6$ mm) and the subsequent graupel/snow pellet Period E ($D_0 \leq 3$ mm). This change would correspond to an estimated bulk density increase of 0.05 g cm^{-3} (Fig. 1).

b. Comparison of the measured and calculated Z_H and Z_{DR}

Figure 4 shows time histories of measured and computed Z_H and Z_{DR} . The radar measurements were averaged over a 1-km radius circle centered at the disdrometer site. [The 0.5° and 1.5° elevation radar beams were 408 and 740 m above the disdrometer,

Table 1: Summary of hydrometeor observations taken at the disdrometer site. Particle types are listed from most to least common. Typical aggregate sizes (mm), percentage of total particles identified as aggregates, and degree of riming (none, light, moderate, heavy) are noted. Temperature ranges are from a sensor mounted on the disdrometer.

	Time (UTC)	Crystals	Aggregates	Temperature ($^\circ\text{C}$)
A	0000-0100	Rain	—	5.5-7
B	0100-0120	Rain mixed with ice pellets	None	0.5-5.5
C	0120-0145	ice pellets	3-8 mm 30 % light	0.5
D	0145-0220	dendrites, plates, stellars	3-10 mm 40 % light to mod.	0.1
E	0220-0400	irregular snow, lump graupel	2-5 mm 5-20 % light	-0.5-0.1

respectively. These heights correspond to 1.93 and 2.26 km MSL.] The RHs of Z_H and Z_{DR} were uniform in the horizontal; thus, the comparisons do not take in account particle trajectories. Figure 5 displays the time evolution of Z_H and Z_{DR} profiles at the disdrometer site.

The Z_H retrievals with the disdrometer data in Period A are slightly less than the radar measurements. The Z_H cross section in the early rain stage shows an elevated layer of maximum reflectivity at ~ 3 km (Fig. 5). Evaporation at low levels may account for the offset between the estimated and measured values. When Z_H is computed assuming that all particles are snow in the rain period (Period A), the retrievals are significantly less than the measurements, reflecting the dependency of Z_H on the hydrometeor dielectric constant.

Agreement between the measured and computed Z_H are excellent during the snow period (after 0100 UTC). Well-matched retrievals in Period B, when using the snow scattering amplitude, come from the fact

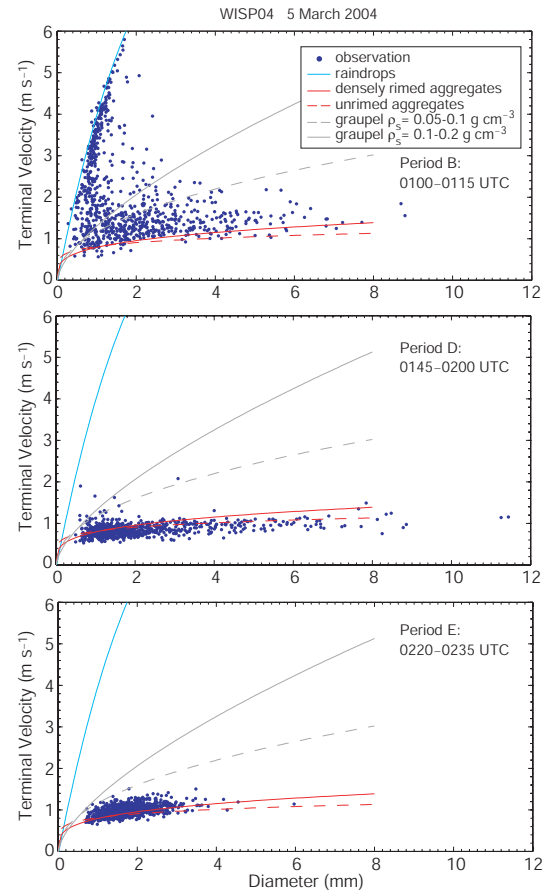


Figure 2: One-second averages of particle terminal velocity versus diameter for time segments in Period B (top), Period D (middle), and Period E (bottom). Hydrometeor observations during these time periods are indicated in Table 1. The terminal velocity relation for rain is from Brandes et al. (2002). The relations for graupel and snow aggregates are from Locatelli and Hobbs (1974).

that return signals from large, low density aggregates dominate over the returns from the smaller raindrops and ice pellets. An overall reduction in the particle size and an associated decrease in snowfall rate (Period D and Period E) coincides with a Z_H reduction of 10 dBZ or more throughout the cloud (Figs. 4 and 5).

Similarly, Z_{DR} calculations and measurements for the respective rain and snow phases show good agreement (Fig. 4). As with Z_H , Z_{DR} retrievals based on raindrop scattering amplitudes exceed the measurements during the rain-snow transition period. Correspondence for the snow period is attributable in large part to accounting for particle density changes. Small Z_{DR} is associated with low density aggregates in Period B through Period D. The measured and computed Z_{DR} values slightly increased when the number of aggregates significantly decreased and small graupel and snow pellets with higher density became dominant (Period E). This calculated Z_{DR} increase was not observed if the bulk density was fixed at a constant value of 0.05 g cm^{-3} .

Changes in precipitation microphysics can be inferred from Fig. 5. An overall decrease in Z_{DR} and increase in Z_H toward ground in Period B through Period D indicate that aggregation was taking place in the lower half of the cloud layer (below 3-3.5 km MSL, Fig. 5). Z_{DR} greater than 0.5 dB in the upper half of the cloud between 0130 and 0245 UTC suggests that these particles were more pristine. The temperature at cloud top was at approximately -13°C ; thus the presence of plates and dendritic ice crystals is plausible (Magono and Lee 1966). Later, Z_{DR} increases and Z_H decreases in the lower half of the cloud layer (see for example below 3 km MSL after 0200 UTC) consistent with an increase in bulk density as detected by the disdrometer. Perhaps, the ice crystals originating at higher levels between 0130 and 0245 UTC arrived at the surface as graupel and heavily rimed ice crystals. A general decrease in Z_{DR} from 0.3 to 0.1 dB between the 1.5 and 0.5° elevation scans (Fig. 4) can be interpreted as evidence that particles were more oblate at higher elevations and that riming was taking place between the two scan levels causing the particles to become less oblate in the mean as they fell.

5. Retrievals of snow particle size distributions

Measurements of Z_H and Z_{DR} have been used previously to infer raindrop size distributions. Here, the retrieval procedure of Zhang et al. (2001) is applied to the data from Periods B-E. The retrievals are based on the definitions of Z_H and Z_{DR} expressed in terms of the Gamma PSD parameters [concentration parameter (N_0), shape factor (μ), and slope (Λ)], particle backscattering amplitudes, and an empirical relation between μ and Λ . The relation between μ and Λ was derived from the disdrometer observations in Fig. 1. The governing PSD parameters were obtained from the 2nd, 4th, and 6th moments of PSDs. For this dataset, μ and Λ are related by,

$$\mu = -0.004992\Lambda^2 + 0.7982\Lambda - 0.6658 \quad (3)$$

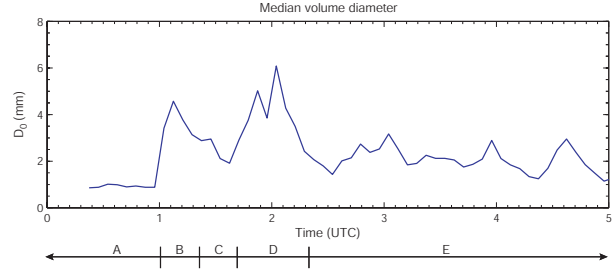


Figure 3: Changes in D_0 with time from 5-minute PSDs. Periods A-E are marked at the bottom.

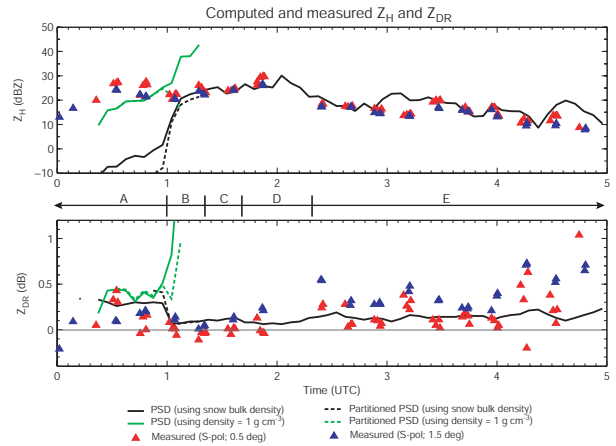


Figure 4: Time histories of measured and disdrometer-based estimates of Z_H (top) and Z_{DR} (bottom). Solid lines are the disdrometer-based estimates of Z_H and Z_{DR} based on 5-min PSDs assuming all particles are either snow (black) or rain (green). Dotted lines during the mixed-phased precipitation represent raindrops or snow particle contributions to the measurements. The disdrometer measurements of particle terminal velocities were used to partition data into raindrop and snow particle categories (e.g., Fig. 2, top frame).

Figure 6 compares the 3rd moments and total particle concentration (N_T) deduced from radar measurements and disdrometer observations. The 3rd moments, related to particle volume, match well between the two datasets. Total concentrations for Periods B and C are consistent with the observations. However, the correlation is poor between the observations and retrievals particularly for N_T from the 0.5° elevation scans after 0220 UTC (Period E) when smaller and denser particles become dominant. Discrepancies may arise partly from the fact that the bulk density rapidly changes toward smaller particle sizes (Fig. 1), the small dynamic range of Z_{DR} for snow, and because the zero-order moment of the PSDs is retrieved from higher moments. Additionally, the large negative bias is due to weak Z_H allowing ground targets to dominate and affect the Z_{DR} measurements. This is

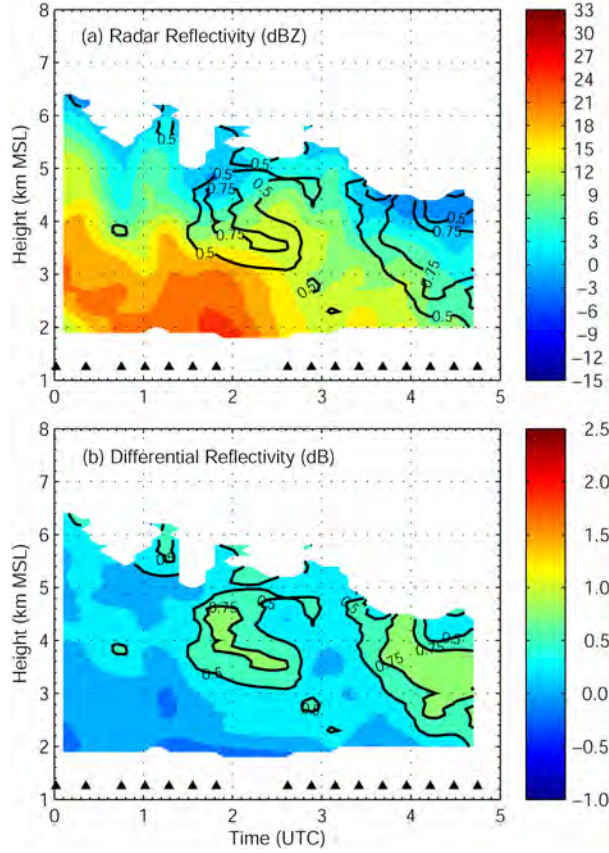


Figure 5: Height-time cross sections of (a) Z_H and (b) Z_{DR} at the disdrometer site based on RHI scans. Measurements were averaged over five azimuthal degrees and 2-km along-radial distances centered at the disdrometer site. Black contours show Z_{DR} of 0.5 and 0.75 dB.

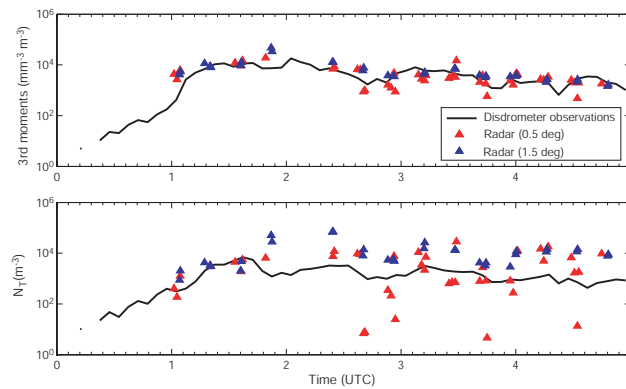


Figure 6: Time histories of the 3rd moments of particle size distributions and total particle concentrations. Solid lines are from disdrometer data and red (blue) triangles are the retrievals from the radar measurements of Z_H and Z_{DR} at 0.5 and 1.5° elevation angles, respectively.

clearly indicated by an increase in scatters in the N_T retrievals from the 0.5° scans.

Sensitivity of the retrieval procedure to ρ_s -D (i.e., scattering amplitudes) and Λ - μ relations were examined through simple sensitivity tests. The results show that an increase in bulk density by 0.02 g cm^{-3} can change the retrievals of the 3rd moments by nearly 50% and the total concentration by 60%. Similar retrieval sensitivity is expected for variations of particle axis ratios as they are also related to the scattering behavior of ice/snow particles.

The changes in the retrievals were less sensitive to variations in the Λ - μ relation. The improvement was most significant for N_T when the distribution was broadened and shifted to larger particle sizes. The root-mean-square error (RMSE) was reduced by 14% to $10.75 \times 10^4\text{ m}^{-3}$. On the other hand, making the PSDs narrower increased the RMSE by 30.4% to $16.43 \times 10^4\text{ m}^{-3}$. The changes were less noticeable for the 3rd moments. Test results suggest that the current retrieval procedure produces too many small, dense particles. Additionally, the results indicate that the technique is more sensitive to the choice of ρ_s -D relation than the Λ - μ relation.

6. Summary and concluding remarks

Radar reflectivity and differential reflectivity were computed from disdrometer data and were compared to radar measurements. The scattering amplitudes for snow particles were derived by exploiting an empirical relationship between particle size and snow bulk density. Overall, the comparisons showed good agreement. Large positive biases in the Z_H and Z_{DR} retrievals during the rain-snow transition period when applying the scattering amplitudes for raindrops disclose the importance of assuming the correct dominant hydrometeor type. The retrievals during the snow period mirrored the changes in hydrometeor habits. Aggregates were associated with small Z_{DR} and large Z_H as expected. An increase in bulk density, as the number of aggregates decreased and that of compact graupel increased, was reflected by a general increase in Z_{DR} and decrease in Z_H throughout the cloud layer. In this case, the use of the size-density relation was important in achieving good agreement between the computed values and measurements.

Reproduction of radar parameters with disdrometer observations is an important initial step in the development of radar-based algorithms for winter precipitation. Well-matched retrievals provide a foundation for reconstructing particle size distributions. Such a capability is required for improving microphysical parameterizations in numerical forecast models and quantifying winter precipitation from radar measurements.

The PSD retrieval procedure based on the measurements of Z_H and Z_{DR} produced an overall agreement in snow particle volume while the total particle concentration was generally overestimated. Results showed that the procedure is sensitive to the empirical relations between the snow bulk density and

particle size. This is in part due to the small dynamic range of Z_{DR} for snow while bulk density rapidly increases for particle sizes <2.5 mm. The retrievals were less sensitive to variations in the relation between slope and shape parameters.

The study of winter precipitation using disdrometer and radar is ongoing. In order to develop radar-based algorithm, examination of more datasets are in order. A field program is being planned to collect additional winter precipitation datasets with a polarimetric radar and 2-D video disdrometer.

Acknowledgement: This research is in response and funding by the Federal Aviation Administration (FAA). The views expressed are those of the authors and do not necessarily represent the official policy or position of the U.S. government. The authors are grateful for Dr. Michael Schoenhuber of the Joanneum Research for his thorough technical advice for the disdrometer operations.

References

- Barber, P., and C. Yen, 1975: Scattering of electromagnetic waves by arbitrarily shaped dielectric bodies. *App. Optics*, **14**, 2864-2872.
- Brandes, E. A., G. Zhang, and J. Vivekanandan, 2002: Experiments in rainfall estimation with a polarimetric radar in a subtropical environment. *J. Appl. Meteor.*, **41**, 674-685.
- Holroyd, III, E. W., 1971: The meso- and microscale structure of Great Lakes snowstorm bands: A synthesis of ground measurements, radar data, and satellite observations. Ph.D. dissertation, State University of New York at Albany, 148 pp.
- Ishimaru, A., 1991: *Electromagnetic Wave Propagation, Radiation, and Scattering*. Prentice Hall, 637 pp.
- Kruger, A., and W. F. Krajewski, 2002: Two-dimensional video disdrometer: A description. *J. Atmos. Oceanic Technol.*, **19**, 602-616.
- Locatelli, J. D., and P. V. Hobbs, 1974: Fall speeds and masses of solid precipitation particles. *J. Geophys. Res.*, **79**, 2185-2197.
- Magono, C., and C. W. Lee, 1966: Meteorological classification of natural snow crystals. *J. Fac. Sci. Hokkaido Univ. Ser. VII*, **2**, 321-362.
- Ryzhkov, A. V., D. S. Zrnić, and B. A. Gordon, 1998: Polarimetric method for ice water content determination. *J. Appl. Meteor.*, **37**, 125-134.
- Zhang, G., J. Vivekanandan, and E. Brandes, 2001: A method for estimating rain rate and drop size distribution from polarimetric radar measurements. *IEEE Trans. Geosci. Remote Sens.*, **39**, 830-841.

FREEZING DRIZZLE DETECTION WITH WSR-88D RADARS

Kyoko Ikeda, Roy M. Rasmussen, and Edward A. Brandes
National Center for Atmospheric Research, Boulder, Colorado

1. Introduction

Freezing drizzle represents a significant in-flight icing hazard and can even cause extensive engine damage to aircraft on the ground. In this paper, we establish a few criteria for detecting freezing drizzle based on WSR-88D radar data. Data analyzed were obtained from a number of freezing drizzle events observed at a selection of operational radar sites. Radar returns are characterized by the areal-average and standard deviation of radar reflectivity factor (reflectivity or Z , hereafter) and the average reflectivity texture.

Freezing drizzle typically forms via the collision-coalescence process rather than the classical melting process. Consequently, a reflectivity bright band is generally absent, making detection difficult. The similarity of echo structures in freezing drizzle and light snow is also a problem for detection techniques based solely on radar reflectivity. Thus, cloud top temperatures are used to gain additional insights regarding cloud microphysical properties.

The ensemble dataset showed that freezing drizzle may be detected from criteria based on cloud top temperatures and radar echo characteristics for single-layered clouds. In other conditions, e.g., in the presence of multiple cloud layers or mixed-phase precipitation, polarimetric-based discrimination of hydrometeors may be more useful because snow particles and drizzle drops have characteristic polarimetric radar returns (Reinking et al. 1997; Ryzhkov and Zrnic 1998).

Section 2 provides a description of the dataset. In Section 3, the evolutions of radar echo signatures in freezing drizzle and light snow from example cases are discussed followed by a summary of the echo signatures from the ensemble dataset. Drizzle detection with a polarimetric radar is discussed in Section 4. A summary and concluding remarks are given in Section 5.

2. Data

Radar data were collected in clear-air mode at 1.5° antenna elevation with the following operational WSR-88D radar systems: Denver, CO (KFTG); Pueblo, CO (KPUX); Goodland, KS (KGLD); Minneapolis, MN (KMPX); Duluth, MN (KDLH); Cleveland, OH (KCLE);

* Corresponding author address: Kyoko Ikeda,
 National Center for Atmospheric Research, P.O. Box
 3000, Boulder, CO 80307
 E-mail: kyoko@ncar.ucar.edu

and Detroit, MI (KDTX). These locations were selected because they are climatologically favorable for freezing precipitation (Bernstein 2000).

Characteristics of radar echo features are summarized with three parameters: (1) average equivalent radar reflectivity (\bar{Z}), (2) reflectivity standard deviation (σ_Z), and (3) average reflectivity texture ($TDBZ$) over a circular area with a radius of 15 km centered at the radar sites. The 1.5° elevation radar beams are about 406 m above the ground at a range of 15 km assuming a standard atmosphere. Thus, in this study, the three parameters are assumed to represent precipitation at the surface. Data from the 1.5° elevation scans are typically less influenced by ground targets. Reflectivity bright bands can potentially skew the statistical values. Generally, the data did not contain a bright band due to their formations via the collision-coalescence process. All statistical values were computed in linear space.

The reflectivity texture ($TDBZ$) is computed from a Radar Echo Classifier algorithm (Kessinger et al. 2003), and is the mean squared difference of the Z at each range gate over a small area. The small areas consist of 5 beams and the number of gates equivalent to 4-km along-radial distances centered at each range gate. $TDBZ$ gives a spatial distribution of smoothness of the Z field. Note that a measure of reflectivity smoothness used for a hydrometeor classification scheme in Ryzhkov et al. (2005) has a slightly different form.

Cloud top temperatures (CTT) are estimated from infrared satellite data. Surface conditions are obtained from the METAR and ASOS reports.

3. Observations with WSR-88D radars

a. Examples cases at KFTG

Radar signatures of freezing drizzle evolve uniquely under various weather conditions. Here, examples are given from freezing drizzle events that occurred over the Front Range regions of Colorado. The precipitation events included a transition from freezing drizzle to light snow allowing to contrast echo features in freezing drizzle and light snow—two precipitation types that are often difficult to distinguish.

Precipitation on 4 March 2003 started as freezing drizzle and later changed to light snow over KFTG. Fig. 1 shows vertical cross sections of reflectivity (Z), vertical gradient of Z (dZ/dh), and $TDBZ$. Shallow orographic cloud produced freezing drizzle between 1100 and 1430 UTC according to the surface

reports. Z was typically less than 0 dBZ during this time segment (Fig. 1a). Small vertical gradients within the cloud layer infer minimal growth of droplets during their descent (Fig. 1b). $TDBZ$ and σ_z at the surface were small, indicating a small spatial variation in the Z field (6.31 dBZ² and 3-5 dBZ, respectively; e.g., Fig. 1c).

A transition from freezing drizzle to light snow was marked with an increase in \bar{Z} to >10dBZ (Fig. 1a; after 1430 UTC), an increase in σ_z by 2 dBZ, and a general increase in $TDBZ$ below 2 km MSL (Fig. 1c). The surface precipitation reports indicated -FZDZSN (freezing drizzle mixed with light snow) consistent with an increasing frequency of ice/snow generating cell-like structures near the cloud top and snow bands over the circular domain. The nucleation of ice likely became more active during this time period as a result of a deepening cloud and cooling of the cloud top from -5°C at 1200 UTC to -15°C by 1500 UTC. Later, a decrease in σ_z by 2-3 dBZ occurred as the low-level cloud became much more stratiform (Fig. 1; after 1700 UTC).

Much stronger Z (i.e., higher snowfall rate) after 1800 UTC near the surface developed in association with an arrival of a Canadian cold frontal cloud (Fig. 1). The frontal cloud appears above the shallow low-level cloud. Freezing drizzle ended by this time as ice/snow particles falling from the seeder cloud depleted the supercooled cloud and drizzle drops (Politovich and Bernstein 1995). In this case, a cooling of the cloud top and the presence of a cloud layer at a higher level eventually suppressed the formation of supercooled drizzle drops.

A shallow orographic cloud behind a cold front produced freezing drizzle at KFTG for more than 24 hours on 30-31 October 2003. The CTTs varied between -10 and -5°C during freezing drizzle. The onset of light snow coincided with a cooling of the cloud top starting at about 1300 UTC on 31 October 2003. The cloud top eventually cooled to nearly -15°C by 1600 UTC. The cloud layer was shallow throughout the event (a depth of 1.6 km). As in the 4 March 2003 case, weak generating cells appeared with the onset of snow, yielding an increase in σ_z . However, the weakening cloud system produced light snow that was barely detectable with the radar. Consequently, \bar{Z} during the periods of freezing drizzle and light snow were similar (Fig. 2). The factors characterizing freezing drizzle in this case were a horizontal homogeneity in the Z field and a relatively warm cloud top.

Freezing drizzle formed behind a quasi-stationary cold front on 4 January 2005. Early freezing drizzle (Fig. 3a) soon became mixed with “very light snow” according to the KDEN surface precipitation reports. This condition continued between 1530 UTC and 2100 UTC and produced hazardous road conditions across the Front Range regions. The radar images consisted of a shallow orographic cloud and scattered mid-level cloud moving with the southwesterly flow (Fig. 3b; also clearly depicted in Fig. 3a). Depletion of supercooled drizzle drops probably took place in limited areas as ice crystals, generated in the mid-level clouds, fell through the low-level cloud layer. Partial depletion of

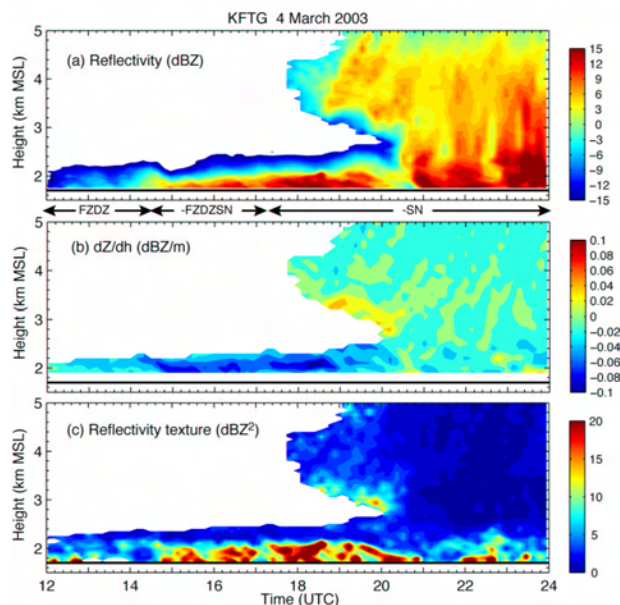


Figure 1: Vertical profiles of (a) radar reflectivity, (b) vertical reflectivity gradient (dZ/dh), and (c) reflectivity texture measured with the KFTG radar on 4 March 2003. Precipitation types are also indicated [freezing drizzle (FZDZ), freezing drizzle and light snow (-FZDZSN), and light snow (-SN)]. The radar parameter profiles were created by averaging values between 55 and 65° azimuthal angles at each gate.

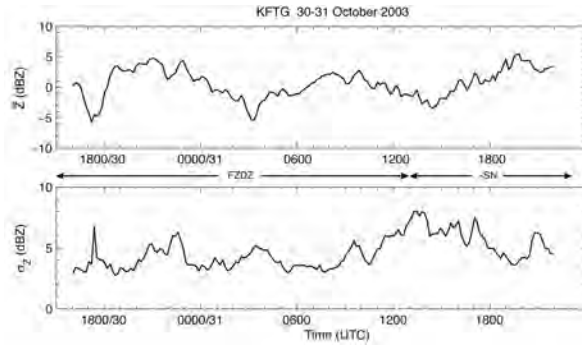


Figure 2: Time histories of average (top) and standard deviation (bottom) of reflectivity measured with the KFTG radar during the 30-31 October 2003 precipitation event.

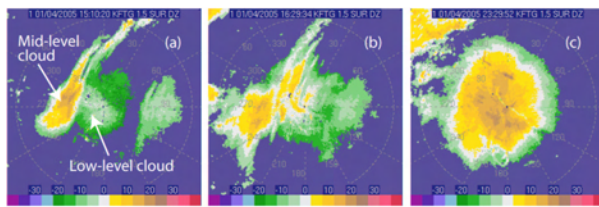


Figure 3: 1.5°-PPI scans at (a) 1510, (c) 1623, and (c) 2323 UTC on 4 January 2005. Range rings are placed every 15 km. From (a) to (c), $\bar{Z} = -3.8, 2.7$, and 14.4 dBZ, and $\sigma_z = 7.4, 5.0$, and 4.3 dBZ.

drizzle drops in the feeder cloud (low-level cloud) in part produced a less uniform Z field with a relatively large values of Z (Fig. 3b) compared with the previous two cases. These values are also large in this case because the mid-level cloud moved over the 15-km radius circular domain.

Freezing drizzle ended, and light snow continued after 2200 UTC. Stratiform precipitation developed by this time returning to a Z field with a smooth texture and small σ_z (Fig. 3c). Although the

$TDBZ$ and σ_z were generally similar to or smaller than those of the earlier freezing drizzle stage, CTTs were much less ($< -30^\circ\text{C}$), the Z rapidly increased toward ground, and the Z was higher near the surface (> 10 dBZ)—all of which are typically not observed in freezing drizzle.

The cloud system on 16 February 2005 over regions surrounding Pueblo, Colorado also consisted of a snow generating mid-level cloud that passed over a pre-existing supercooled drizzle cloud. \bar{Z} and σ_z did not significantly change during the precipitation event even though freezing drizzle possibly became mixed with snow as the mid-level cloud passed over the area. A twin-engine airplane approaching the Pueblo Memorial Airport located approximately 33 km southwest of the radar was involved in a fatal crash. In-flight icing that formed as it descended into the supercooled drizzle cloud is currently being considered as one of the causes of the accident. The 4 January

and 16 February 2005 events show difficulty in identifying freezing drizzle based only on Z and CTT in the presence of mixed-phase precipitation and/or multiple cloud layers.

The example cases discussed above showed that weak Z with a small texture and σ_z in the presence of a relatively warm cloud top can suggest the presence of freezing drizzle at the surface (when surface temperature is below freezing). However, the

differences in \bar{Z} , σ_z , and $TDBZ$ in freezing drizzle and light snow are not necessarily consistent from one event to another. For example, the uniformity in the Z field during a light snow event is similar to that in freezing drizzle when snow is from a stratiform cloud with very little cellularity. The detection of freezing drizzle is further complicated in the presence of multiple cloud layers and in mixed-phase precipitation at the surface because the presence of an upper-level cloud layer does not always guarantee the absence of drizzle at the surface; Z near the ground can be as high as 5-10 dBZ; and the satellite-based cloud tops may be much colder than -15°C .

b. Ensemble data

Radar measurements from 17 light precipitation events, including freezing drizzle and light snow, obtained from a selection of radar systems (Section 2) are examined here. CTTs from satellite (available every 15 or 30 minutes) were interpolated in time to find temperature associated with radar scans in 6-minute intervals. $TDBZ$ is not shown here because the variations of $TDBZ$ with CTT are similar to that of σ_z with CTT.

The ensemble data showed that freezing drizzle mostly occurred when only a low-level cloud layer with $CTT > -20^\circ\text{C}$ was present. For relatively warm precipitation events ($CTT > -10^\circ\text{C}$), freezing drizzle was typically associated with a small σ_z in order of 4 dBZ (Fig. 4). Although only 18 data points are from light snow cases compared with 110 points for freezing drizzle, this is about 3 dBZ lower than in light snow for similar magnitudes of Z . A smoother Z field in freezing drizzle is largely due to a stratiform nature of the drizzle cloud. For cold precipitation events ($CTT < -10^\circ\text{C}$), \bar{Z} remains low (~ 0 dBZ) in freezing drizzle; whereas \bar{Z} in light snow increases (Fig. 5). The larger Z associated with light snow is due to the fact that ice generation occurs rapidly near the cloud top, and particles grow to appreciable sizes as they descend through the cloud. As a consequence, the vertical gradient of Z is larger than that in freezing drizzle. However, the horizontal uniformity in the two precipitation types is similar. Smooth Z fields in light snow cases come from stably stratified clouds as on 4 March 2003 (1700-1800 UTC). Ice generating cells and snow bands were typically absent in these clouds.

Consistent with findings from the case studies presented in the previous section, the ensemble data indicate that a freezing drizzle detection scheme first should associate a weak and a relatively smooth Z field

with freezing drizzle when only a low-level cloud layer is present. Then it should increase the likelihood of freezing drizzle when σ_z is <5 dBZ in the presence of a single cloud layer in the warm regime and when \bar{Z} is <5 dBZ in the cold regime.

The values of \bar{Z} and σ_z in freezing drizzle and light snow overlap significantly when multiple cloud layers are present (Fig. 6) as on 4 January 2005. Examination of individual cases indicated that small \bar{Z} and σ_z in freezing drizzle (~ 0 dBZ and <5 dB, respectively) appear to occur when there is a significant wind shear between the low-level cloud layer and the overlying cloud layer. Perhaps, the seeder-feeder mechanism was not effective in glaciating the drizzle layer. On the other hand, freezing drizzle associated with a less uniform Z field and larger \bar{Z} occurred when the radar echo top heights were not uniform across the 15-km radius domain. CTT associated with the cloud layer overlying the drizzle cloud was as cold as -50°C in some cases. The data show that detection criteria based only on Z and CTT are difficult to establish.

4. Observations with a polarimetric radar

Lead by the National Weather Service, a program to add polarimetric capability to the network of WSR-88Ds is currently underway (Ryzhkov et al. 2005). Because polarimetric measurements are sensitive to particle size, shape, orientation, phase, and density, the measurements would provide more insight regarding particle types than currently available with radar reflectivity alone.

One of the added measurements to the polarimetric WSR-88D is differential reflectivity (Z_{DR}). Z_{DR} is sensitive to particle bulk density, shape, and canting angle and can be interpreted as the reflectivity-weighted mean axis ratio of the illuminated hydrometeors. Z_{DR} is zero for particles that are spherical or have a random distribution of orientations. Z_{DR} typically ranges from 0.2 to 3 dB for rain and increases with drop size and rain intensity. Pristine ice crystals fall with their major axes near horizontal and can have Z_{DR} values as large as 2 to 5 dB depending on crystal type. Z_{DR} for low density aggregates are small (0 to 0.5 dB). Although the capability of Z_{DR} to discriminate between rain and snow has been previously explored (e.g., Ryzhkov and Zmic 1998), there has been few detailed studies contrasting return signals from drizzle and snow (e.g., Reinking et al. 1997; Reinking et al. 2002). Here, we present measurements of differential reflectivity (Z_{DR}) and reflectivity from horizontal polarization (Z_H) collected from drizzle and light snow with NCAR's S-band polarimetric radar (S-Pol) during the second phase of the Improvement of Microphysical Parameterization through Observational Verification Experiment (Stoelinga et al. 2003).

Figures 7 and 8 show scatter plots of Z_H and Z_{DR} measurement pairs and the distributions of Z_{DR} just below and above the melting layer. The measurements were obtained in light orographic precipitation. The Z_H

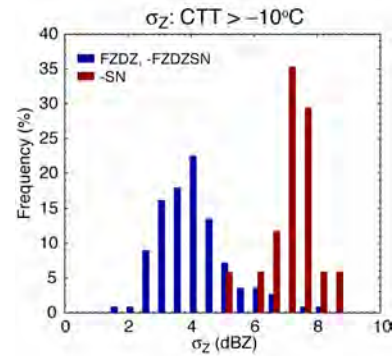


Figure 4: Frequency distribution of σ_z for warm events with a single low-level cloud layer.

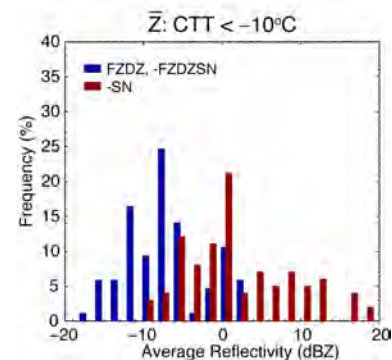


Figure 5: Frequency distributions of \bar{Z} in cold events with a single low-level cloud layer.

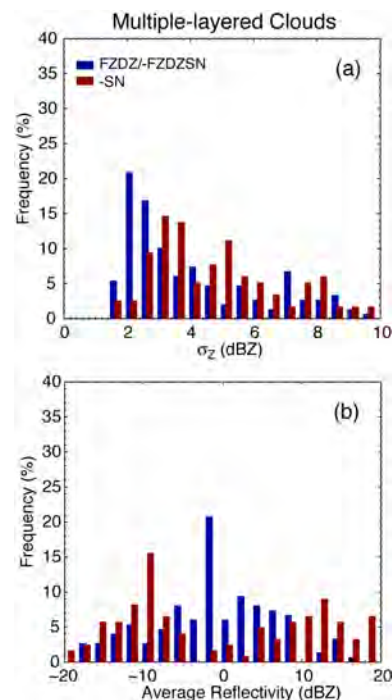


Figure 6: Frequency distribution of (a) σ_z and (b) \bar{Z} for the cases with multiple cloud layers.

and Z_{DR} are small below the melting layer suggesting that the drops were small (Fig. 7a). The absence of a bright band in the reflectivity cross sections also indicated that drops below the melting layer were probably drizzle. The Z_{DR} distribution for drizzle is strongly peaked near 0 dB (Fig. 7b) because they are essentially spherical. Although this is not a case of freezing drizzle, the radar returns are similar. Compared to drizzle, Z_{DR} is higher in the ice layer (~ 0.6 dB) for similar magnitude of Z_H , indicating that the particles are less spherical in the mean (Fig. 8). A broad distribution of Z_{DR} in the ice layer was also common among datasets examined in this study. These differential Z_{DR} signatures in drizzle and snow give prospects of enhanced freezing drizzle detection with a polarimetric WSR-88D.

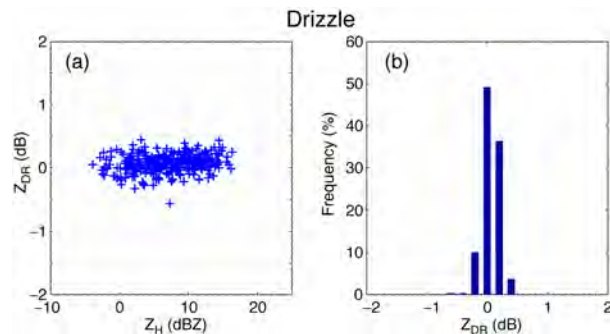


Figure 7: (a) Scatter plot of Z_{DR} and Z_H from a selected area below the melting layer, and (b) a frequency distribution of Z_{DR} . The measurements were collected between 1202 and 1204 UTC on 28 November 2001 during IMPROVE II.

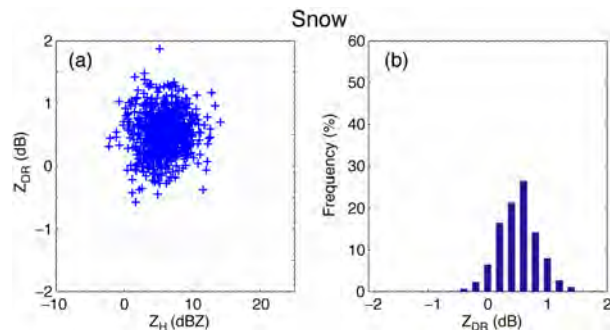


Figure 8: Same as Fig. 7 but for measurements above the melting layer.

5. Summary and concluding remarks

The WSR-88D radar measurements obtained in freezing drizzle were discussed and compared to the often-similar measurements of light snow in order to develop a radar-based algorithm to detect freezing drizzle. The ensemble data indicated that the precipitation can be classified as freezing drizzle using

CTT and Z-based parameters (\bar{Z} , σ_Z , and $TDBZ$) when only a low-level cloud layer is present. Although light

snow can produce similar magnitudes of Z , the Z field is typically more horizontally uniform in freezing drizzle during warm events ($CTT > -10^\circ\text{C}$). The average Z near the surface and the rate of Z increase toward ground are larger in cold events ($CTT < -10^\circ\text{C}$) for light snow, as ice generation becomes active near the cloud top and ice crystals rapidly grow; whereas, the radar returns in freezing drizzle continue to have a relatively weak Z . Freezing drizzle formation becomes limited with much colder CTTs ($< -20^\circ\text{C}$). Radar echo patterns for freezing drizzle largely overlapped with light snow when multiple cloud layers were present. In these cases, CTT and Z were not sufficient to discriminate between freezing drizzle and snow.

Comparisons of Z_H and Z_{DR} pairs in drizzle and ice layers revealed that Z_{DR} in the drizzle layer differ in two ways: (1) it is smaller for a specified Z_H ; and (2) the range of values at a specific Z_H is narrow. The different signatures in drizzle and light snow should enhance freezing drizzle detection when polarimetric WSR-88Ds become available. Polarimetric measurements (not only Z_{DR}) add more insight regarding the particle types and are particularly useful for precipitation events in the cold regime or with multiple cloud layers in which cases the particle discrimination criteria based on CTT and Z do not apply.

Acknowledgement: This research is in response and funding by the Federal Aviation Administration (FAA). The views expressed are those of the authors and do not necessarily represent the official policy or position of the U.S. government.

References

- Bernstein, B. C., 2000: Regional and local influences on freezing drizzle, freezing rain, and ice pellet events. *Wea. Forecasting*, **15**, 485-508.
- Geresdi, I., R. Rasmussen, W. Grabowski, and B. Bernstein, 2005: Sensitivity of freezing drizzle formation in stably stratified clouds to ice processes. *Meteorol. Atmos. Phys.*, **88**, 91-105.
- Kessinger, C., S. Ellis, and J. Van Andel, 2003: The radar echo classifier: A fuzzy logic algorithm for the WSR-88D. Preprints, *3rd Conference on Artificial Applications to the Environmental Science*, Long Beach, CA, Amer. Meteor. Soc.
- Politovich, M. K., and B. C. Bernstein, 1995: Production and depletion of supercooled liquid water in a Colorado winter storm. *J. Appl. Meteor.*, **34**, 2631-2648.
- Reinking, R. F., S. Y. Matrosov, B. E. Martner, and R. A. Kropfli, 1997: Dual-polarization radar to identify drizzle, with applications to aircraft icing avoidance. *J. Aircraft*, **34**, 778-784.
- _____, R. A. Kropfli, and B. W. Bartram, 2002: Evaluation of a 45° slant quasi-linear radar polarization state for distinguishing drizzle droplets, pristine ice crystals, and less regular ice particles. *J. Atmos. Oceanic Technol.*, **19**, 296-321.

- Ryzhkov, A. V., and D. S. Zrníc, 1998: Discrimination between rain and snow with a polarimetric radar. *J. Appl. Meteor.*, **37**, 1228-1240.
- , T. J. Schuur, D. W. Burgess, P. L. Heinselman, S. E. Giangrande, and D. S. Zrníc, 2005: The Joint Polarization Experiment: Polarimetric rainfall measurements and hydrometeor classification. *Bull. Amer. Meteor. Soc.*, **86**, 809-824.
- Stoelinga, M. T., and co-authors, 2003: Improvement of microphysical parameterization through observational verification experiment. *Bull. Amer. Meteor. Soc.*, **84**, 1807-1826.

NSSL Dual-pol FAA Report February 2006

Introduction

The emphasis of the dual-pol studies in the last quarter of 2005 was on mixed-phase precipitation and polarimetric analysis of frozen hydrometeors in the clouds. Cold-season clouds that frequently produce icing hazard are often characterized by weak radar echo. If signal-to-noise ratio drops below 20 dB, then two important polarimetric variables, differential reflectivity Z_{DR} and cross-correlation coefficient ρ_{hv} , become biased by noise. All microphysical inferences in weakly reflected mixed-phase clouds critically rely on unbiased estimates of Z_{DR} and ρ_{hv} . In the first section of the report, the newly introduced “1-lag” method for noise correction is briefly described and compared to the conventional technique which implies direct measurements of noise.

A new method for polarimetric detection of the melting layer has been recently introduced at NSSL (Giangrande et al. 2005). In the second section of the report, the results of validation studies for the freezing level determination are summarized. Finally, in the third section, we illustrate unique capabilities of the dual-polarization radar to delineate rain-snow boundary and to identify the areas of intense aggregation in winter clouds using the C-band polarimetric radar.

I. Correction of Z_{DR} and ρ_{hv} for noise.

Configuration with Simultaneous transmission and reception of electromagnetic waves with **H**orizontal and **V**ertical polarizations (**SHV** configuration) has been chosen for a polarimetric prototype of the WSR-88D weather radar. Six radar moments are measured with the radar in each radar resolution volume: reflectivity, Z , the Doppler velocity, v , spectrum width, σ_v , differential reflectivity, Z_{DR} , differential phase, ϕ_{dp} , and modulus of the copolar correlation coefficient, ρ_{hv} . The first three values are the base radar moments of the WSR-88D, the latter three are base polarimetric variables.

On the WSR-88D, the base radar moments are calculated at signal-to-noise ratios, SNR, larger than 3.5 dB. The same threshold should be applied for the polarimetric variables. That requires considering polarimetric estimates at low SNR. The polarimetric estimates are prone to noise bias at SNR less than 15 dB. This vulnerability becomes more pronounced with range due to the drop of the scattered power with distance. On the legacy WSR-88D, the radar variables are measured starting with signal-to-noise (SNR) ratios 3.5 dB. The polarimetric moments should also be measured at such low SNR.

Uncertainty of the system noise level

In the SHV, differential reflectivity, the differential phase and modulus of the copolar correlation coefficient are calculated as:

$$\hat{Z}_{DR} = 10 \log \frac{\hat{P}_h - N_h}{\hat{P}_v - N_v}, \quad (1)$$

$$\hat{\varphi}_{dp} = \arg(\hat{R}_{hv}), \quad (2)$$

$$\hat{\rho}_{hv} = \frac{|\hat{R}_{hv}|}{[(\hat{P}_h - N_h)(\hat{P}_v - N_v)]^{1/2}}, \quad (3)$$

where the circumflex denotes estimates, \hat{P}_h and \hat{P}_v are the estimates of the powers in the channels for horizontally (h) and vertically (v) polarized waves, N_h and N_v are the mean noise powers in the channels, and \hat{R}_{hv} is the estimate of the copolar correlation function that is calculated from complex voltages $e_m^{(h)}$ and $e_m^{(v)}$ in the H and V channels as

$$\hat{R}_{hv} = \frac{1}{M} \sum_{m=1}^M e_m^{(h)} e_m^{(v)*}, \quad (4)$$

M is the number of samples used in the estimate, m numerates the samples, and the asterisk denotes complex conjugate. It follows from (1) and (3) that ZDR and ρ_{hv} depend on the weather signal powers in the channels \hat{S}_h and \hat{S}_v which are obtained as:

$$\hat{S}_h = \hat{P}_h - N_h, \quad \hat{S}_v = \hat{P}_v - N_v. \quad (5)$$

We will refer to relations (1) to (3) as conventional estimates.

System noise is measured on WSR-88D at elevation 22° . Then this noise is used by the system at low elevations in the presence of precipitation during the whole volume coverage pattern. It is known that system noise is different for different elevations due to ground noise and thermal noise from precipitation. Internal system noise also varies over time. It is seen from (1) and (3) that if the noise powers used by the system differ from true noise, the estimates of ZDR and ρ_{hv} are biased. Consider briefly the following three source that change system noise: thermal radiation from precipitation and the ground, time variations of system gains in the channels, and electromagnetic emission from thunderstorms.

It is well known that thermal radiation coming to the radar antenna from precipitation increase the noise level and this increase depends on attenuation at a given direction. On polarized WSR-88D KOUN, we have observed noise increase of 0.8 dB. At S-band, attenuation can reach 8 dB and corresponding noise increase can exceed 1 dB. Let N_a be the power of additional noise, then the noise increase of 0.8 dB (i.e., $10\log[(N_h + N_a)/N_h] = 0.8$) corresponds to $N_a/N_h = 0.2$ and 1.5-dB increase corresponds to $N_a/N_h = 0.4$. Here we consider noise increase due to thermal radiation from the ground and precipitation up to 1.5 dB. Thermal radiation from the ground also contributes to system noise at low elevations.

Time variations of the system gain cause noise variations. Fig. 1 presents an example of noise records in the KOUN's H channel. With the antenna in the park position (azimuth = 0° ; elevation = 22°), 400 consecutive range gates on a radial were split by four equal parts and the mean noise power was calculated for each part with 128 samples for each range gate so that four estimates of the mean noise power were obtained.

This procedure was conducted over time during approximately 50 seconds and the result is presented in the figure in a form of four curves. It is seen that all curves are highly synchronous exhibiting time variations of the gain. Time scale of these variations is of few seconds and variations are about 1 dB. Such variations we observe frequently but not all the time; most of the time they are within 0.5 dB.

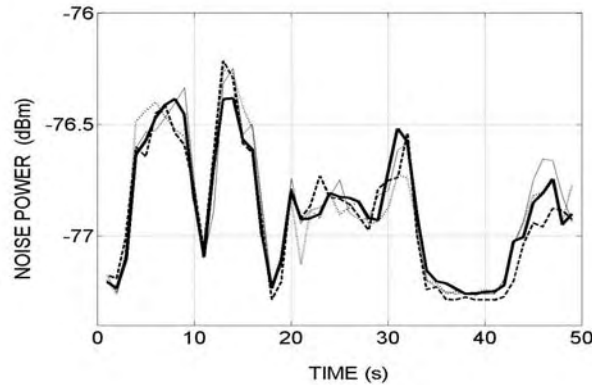


Fig. 1. Temporal variations of the noise level in the horizontal channel of the WSR-88D KOUN. 30 March 2004, 2343 UT.

Thunderstorms emit radiation in a broad frequency band including S-band. This radiation can be intercepted by the antenna and results in excessive noise. Fig. 2 presents two consecutive reflectivity profiles beyond 50 km recorded through a heavy thunderstorm where the noise skirt which is beyond 68 km has not been removed by thresholding. Time interval between the records is 263 ms. The number of samples in the estimate is 256. The gradual increase of the noise level with distance is a result of the range-squared weighting applied in reflectivity calculations. One can see a jump of about 10 dB of the noise level. Such large noise jumps are less frequent than smaller ones. This type of noise is not thermal but because of its broad band it can be considered as white noise for a radar receiver.

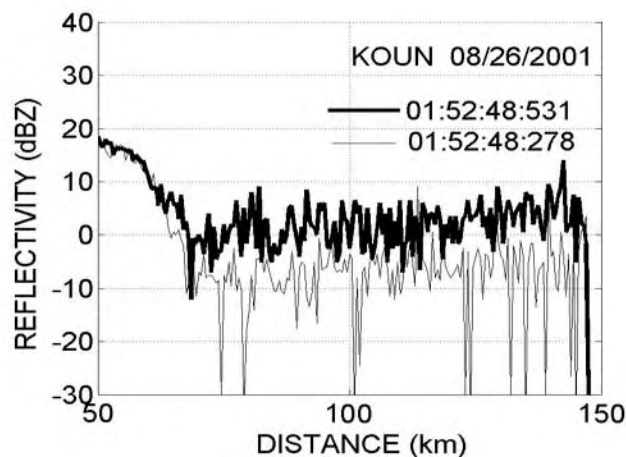


Fig. 2. Two reflectivity profiles on August 26, 2001. Azimuth

is 35.2° and the elevation is 8.6° . UTC time is shown in a format of hour:minute:second:millisecond of the beginning of the records.

We conclude that it is very difficult to confine the radar noise level variations within 1 dB. Uncompensated noise biases the estimates of differential reflectivity and the copolar correlation coefficient. In Fig. 3, biases of Z_{DR} and ρ_{hv} are plotted for $N_a/N_h = 0.2$ and 0.4 that correspond to 0.8 and 1.5 dB of noise increase. It is seen from the figure that biases of differential reflectivity can exceed 0.1 dB in magnitude for SNR less than 13 dB. On KOUN, hardware accuracy of Z_{DR} measurements is 0.1 dB (Zrnic et al. 2005) so that noise variations less than 1.5 dB can bias Z_{DR} by a larger value than hardware uncertainties. The copolar correlation coefficient is more sensitive to uncompensated noise: its bias can be 0.005 in magnitude for SNR as high as 18 dB. At SNR about 3.5 (low limit of the WSR-88D measurements), 1.5 dB of noise deviation can bias Z_{DR} and ρ_{hv} much larger than the hardware accuracy. Thus, it is desirable to devise algorithms immune to the level of system noise. Such estimators are considered in the following section.

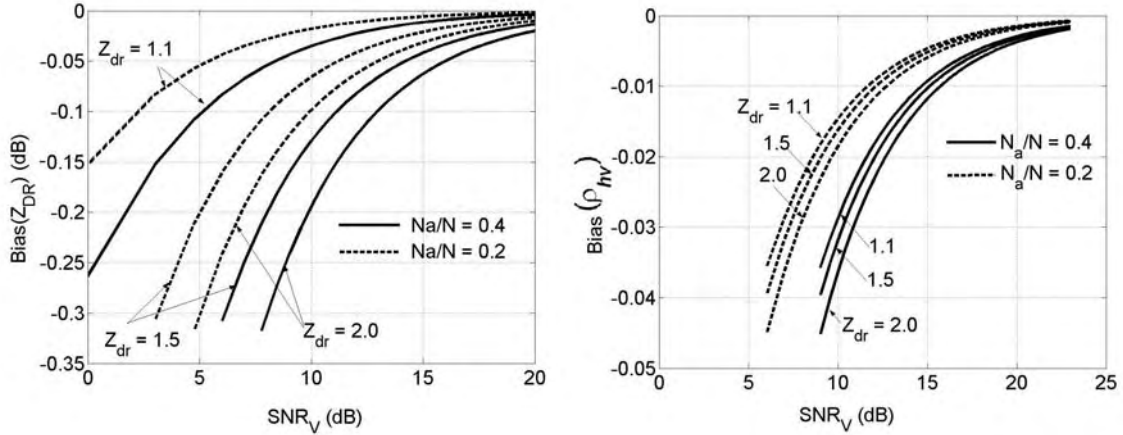


Fig. 3. Biases of the \hat{Z}_{DR} (left) and $\hat{\rho}_{hv}$ (right) estimates due to additional white noise N_a for equal noise levels $N_h = N_v = N$ and two N_a/N ratios.

Z_{DR} and ρ_{hv} estimates free from noise bias

We write the correlation functions for the H and V channels at lag T as:II. Melting layer detection

$$R_h(T) = S_h \rho^{(h)}(T) \exp(j\pi v_h / v_a), \quad (6a)$$

$$R_v(T) = S_v \rho^{(v)}(T) \exp(j\pi v_v / v_a), \quad (6b)$$

where the subscripts and superscripts h and v denote the parameters that are calculated using the pulse trains in the H and V channels, T is the pulse repetition interval ($T =$

1/PRF), v_a is the unambiguous velocity ($v_a = \lambda/4T$, λ is the wavelength), $\rho^{(h)}(T)$, $\rho^{(v)}(T)$ are the temporal correlation coefficients, and j is imaginary one. Values without the circumflex are true means, for instance $\langle \hat{R}_h(mT) \rangle = R_h(mT)$, where the brackets stand for ensemble average.

Copolar correlation function $R_{hv}(nT)$ can be calculated for arbitrary lag n similarly to (4). Assuming that ρ_{hv} is not dependent on time and is determined by average shapes, the mean canting angles of the hydrometeors, and the drop size distribution we write

$$R_{hv}(T) = (S_h S_v)^{1/2} \rho_{hv} \rho^{(hv)}(T) \exp(j\pi w_{hv} / v_a + j\phi_{dp}), \quad (7a)$$

$$R_{hv}(0) = R_{hv} = (S_h S_v)^{1/2} \rho_{hv} \exp(j\phi_{dp}), \quad (7b)$$

where time variations of shapes and the canting angles affect the temporal correlation coefficient $\rho^{(hv)}(T)$, and the subscript and superscript hv mean that the parameters are calculated using the pulse trains in both H and V channels. To shorten the notations we write $R_{hv}(0) = R_{hv}$. The modules of functions (6) and (7) do not depend on the Doppler velocities:

$$\begin{aligned} |R_h(T)| &= S_h \rho^{(h)}(T), & |R_v(T)| &= S_v \rho^{(v)}(T), \\ |R_{hv}(T)| &= (S_h S_v)^{1/2} \rho_{hv} \rho^{(hv)}(T), \end{aligned} \quad (8)$$

Three temporal correlation coefficients in the latter equations can differ. They are functions of the spectral width and thus depend on the velocity spread, oscillations and wobbling of the hydrometeors. Primary contribution to the spectral width is the spread of velocities, contributions from wobbling and oscillations are small. That is why signals in the two SHV channels are highly correlated which is well known and we can write $\rho^{(h)}(T) = \rho^{(v)}(T) = \rho^{(hv)}(T) = \rho(T)$. Then Z_{DR} and ρ_h can be obtained from (8) as:

$$Z_{DR} = 10 \log \frac{S_h}{S_v} = 10 \log \frac{|R_h(T)|}{|R_v(T)|}. \quad (9)$$

$$\rho_{hv} = \frac{|R_{hv}(T)|}{(|R_h(T)| |R_v(T)|)^{1/2}}. \quad (10)$$

The modules in (9) and (10) do not depend on noise so that these two estimates are not biased by white noise.

In Fig.4, Z_{DR} fields calculated with the conventional and 1-lag estimators are presented. The figure is a vertical cross-section of widespread light rain. The following two features follow from the figure. 1) The field obtained with the 1-lag estimator is larger than the field of the conventional algorithm. The latter was obtained with usual SNR threshold for reflectivities, i.e., 2 dB. Experiments with thresholding of the 1-lag estimates have shown that corresponding SNR threshold is 0 dB. Lower SNR thresholds produce larger fields. The lowering of SNR thresholds at the 1-lag estimator is possible because the algorithm is immune to noise bias. 2) It is seen from Fig. 4 that the

conventional Z_{DR} are negative at the top of the cloud. That indicates overestimation of the noise level in the horizontal channel or underestimation of noise in the vertical channel. Combined analysis of Z_{DR} and ρ_{hv} fields shows that noise in the horizontal channel is overestimated. The 1-lag Z_{DR} estimator (bottom image in Fig.4) has no such noise bias.

In Fig. 5, the fields of the copolar correlation coefficients obtained with the conventional and 1-lag estimators are presented. Due to overestimation of noise in the horizontal channel, the conventional ρ_{hv} are equal to 1 at the top of the cloud. In contrast, the 1-lag estimator produces more realistic coefficients: they are high but slightly lower than 1. It is also seen from Fig.5 that the bottom image obtained with the 1-lag estimator is larger than the top one corresponding to the conventional algorithm. This is a consequence of the fact that the 1-lag algorithm is free from noise bias.

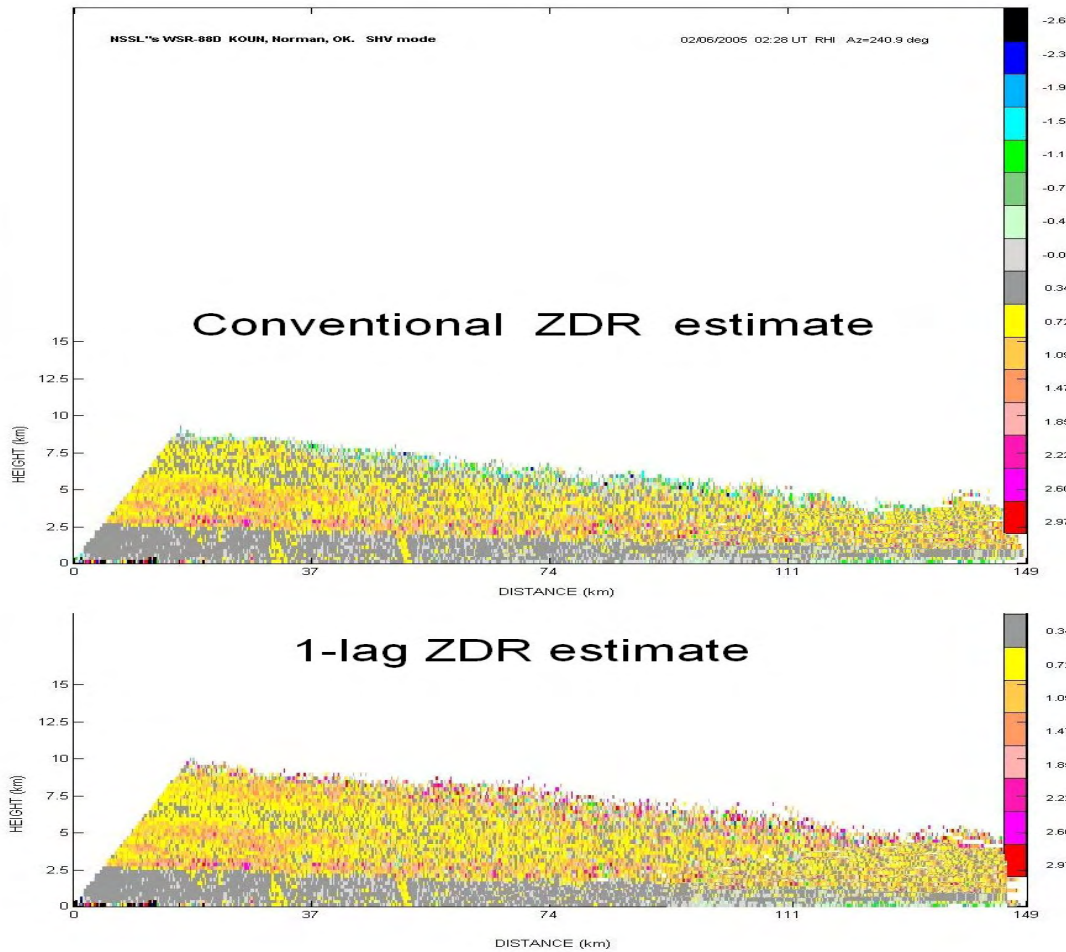


Fig. 4. Z_{DR} fields obtained with the conventional (top) and 1-lag (bottom) estimators on 6 February, 2005 at 02:28 UTC. Azimuth is 241 deg.

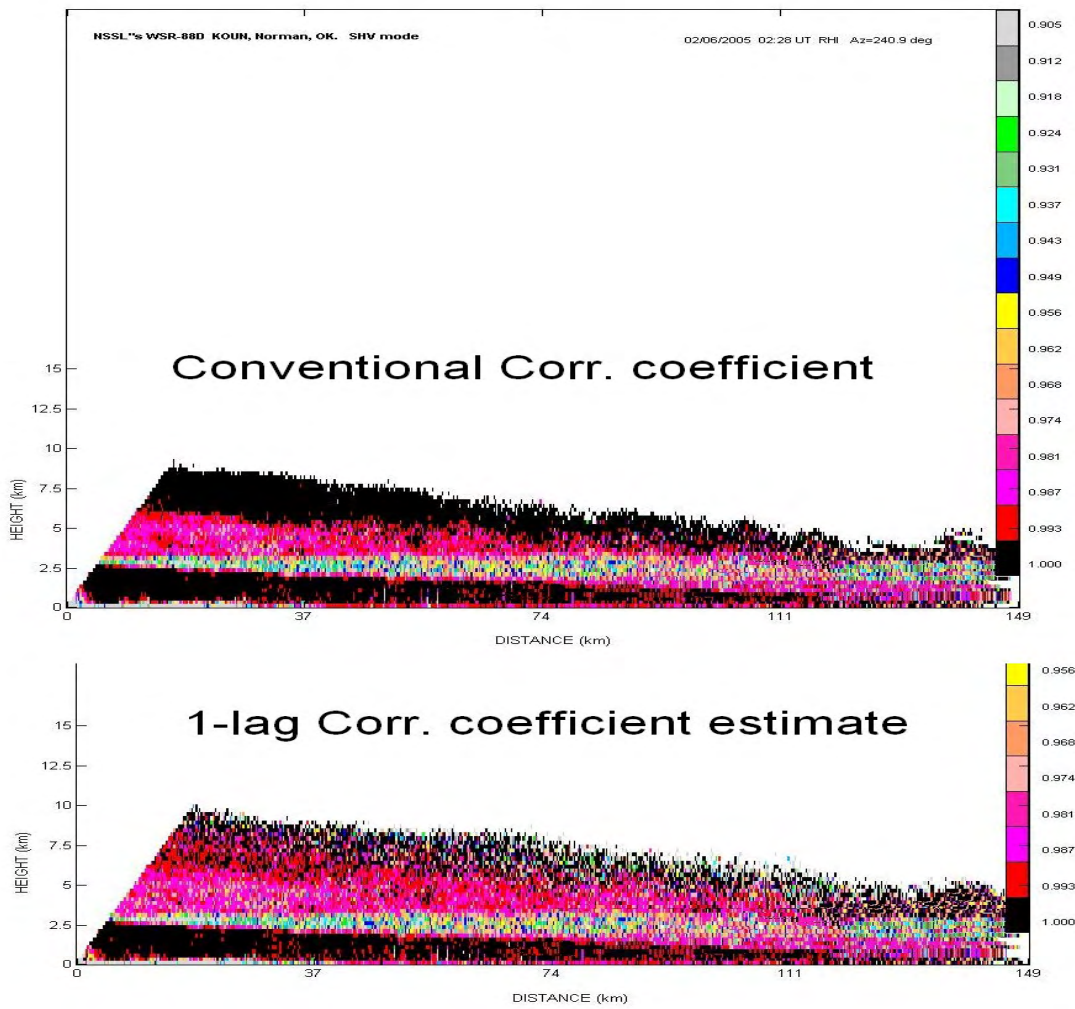


Fig. 5. Copolar correlation coefficients obtained with the conventional (top) and 1-lag (bottom) estimators on 6 February, 2005 at 02:28 UTC. Azimuth is 241 deg.

II. Melting layer detection

The melting layer detection algorithm determines the top and bottom of the melting layer. The top of the melting layer coincides with the freezing level or the height of the 0°C isotherm. The bottom of the melting layer represents the height where all wet snowflakes melt into raindrops. This usually occurs where the environmental temperature is about 3 - 5°C. In order to evaluate the accuracy of the freezing level designation, we compared the results of dual-pol retrieval with the output of the RUC model and sounding data using several consecutive hours of observations for different storms.

Examples of such comparisons are displayed in Fig. 6 where crosses indicate the heights of the top and the bottom of the melting layer retrieved from the data collected by the KOUN WSR-88D radar, triangles stand for the height of the freezing level obtained

from the RUC model, and diamonds designate the height of the freezing level from soundings.

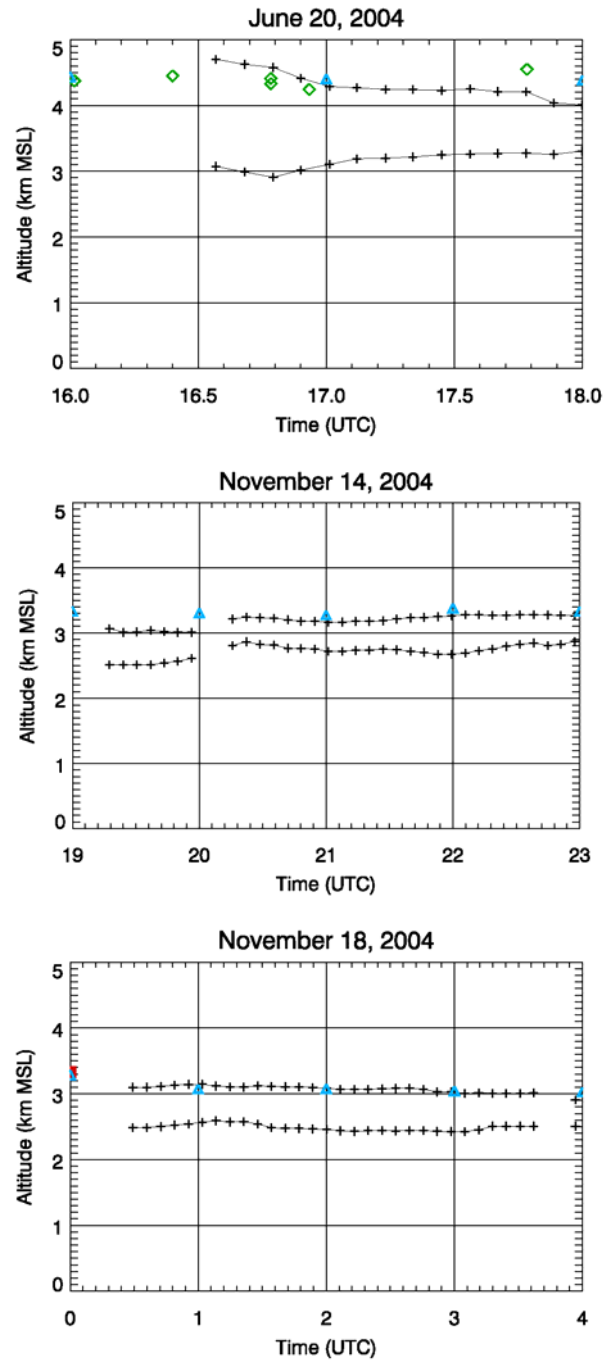
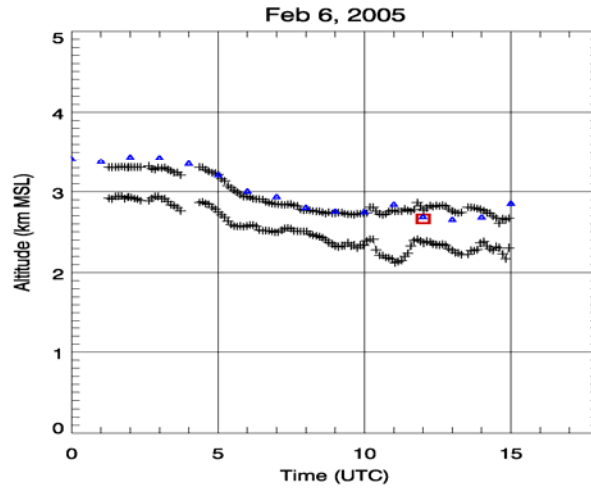


Fig. 6 Temporal evolution of the top and bottom of the melting layer for three storms as revealed by the KOUN WSR-88D polarimetric radar (crosses), from the RUC model (triangles), and atmospheric soundings (diamonds).

The agreement between all three estimates of the freezing level height is within 100 – 200 m. In the examples in Fig.6, temporal changes in the freezing level height are relatively small. In the case of the February 6, 2005 storm (Fig. 7a), both polarimetric radar and the RUC model reveal significant subsidence of the freezing level that is confirmed by independent sounding measurement shown by red rectangle.

(a)



(b)

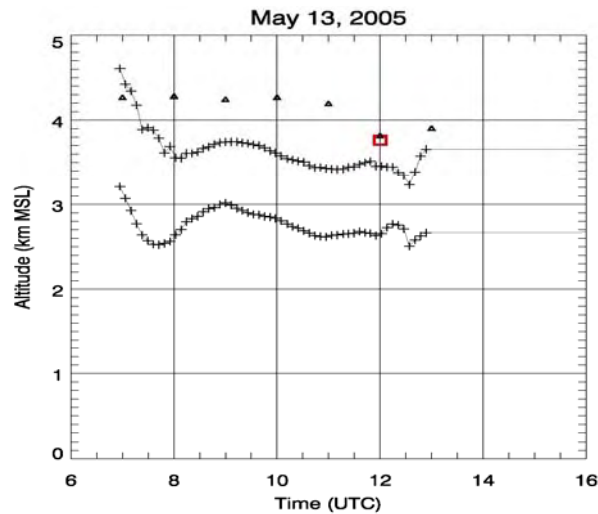


Fig. 7. Same as in Fig. 6, but for the cases with descending melting layer.

Fig. 7b illustrates the case of a mesoscale convective system on May 13, 2005 when, according to the polarimetric data, the melting layer descends as a result of air cooling due to intense evaporation / melting and precipitation loading. Such a descent, however, is not captured by the RUC model (triangles) because of a possible deficiency of the model in the case of a strong MCS. The heights of the freezing level (top of the melting layer) derived from the radar and RUC model differ by 500 – 700 m between 8Z and 12 Z. In this case, the radar designation of the melting layer and freezing level might be more reliable than the numerical model output. This is a good example of situation

when assimilation of polarimetric data into numerical model may help to improve its performance.

III. Using polarimetric radar to delineate rain / snow boundary at the surface and to identify the region of snow aggregation.

In two previous quarterly reports, several examples of polarimetric signatures in winter precipitation observed by the KOUN WSR-88D radar have been presented. Recently we got an access to the high-quality C-band polarimetric data from the Environment of Canada. The Canadian radar located in King City near Toronto has a half-a-degree antenna beam and may be considered as a polarimetric prototype of the TDWR radar which is widely used for airport weather surveillance in USA. C-band polarimetric data for 4 winter weather events, 2004/12/23, 2005/11/24, 2005/11/25, and 2006/01/04 are currently being analyzed. Here we present some preliminary results illustrating unique capabilities of the C-band polarimetric radar to detect meteorologically important features in the mixed-phase and snow precipitation events.

The fields of radar reflectivity factor Z , differential phase Z_{DR} , specific differential phase K_{DP} , and cross-correlation coefficient ρ_{hv} at elevation 0.4° are displayed in Fig. 8 at the moment when rain / snow transition line passes over the radar location. This line separating snow in NW sector and rain in SE sector shows up remarkably well in the ρ_{hv} image. The transitional zone is marked by a sharp decrease of the cross-correlation coefficient. The corresponding Z_{DR} associated with wet snow is very high and K_{DP} is modestly high. In dry aggregated snow immediately to the west of the demarcation line, both Z_{DR} and K_{DP} drop almost to zero values. Further to the west, aggregated snow is substituted with denser and lesser aggregated snow with a good proportion of pristine crystals producing much higher Z_{DR} and K_{DP} . The transition between rain and snow as well as changing snow types in the west – east direction was confirmed by surface observations.

The composite RHI of Z , Z_{DR} , K_{DP} , and ρ_{hv} in the azimuthal direction of 310° (Fig. 9) exhibits an elevated layer of high Z_{DR} and low ρ_{hv} at the height interval between 3.5 and 4.5 km. According to soundings, the temperature in this layer was between -5 and -10°C . Only snow on the ground was reported in the corresponding azimuth. Although both Z_{DR} and ρ_{hv} signatures in Fig. 7 resemble the ones typical for the melting layer, they have nothing to do with melting. In fact, they indicate rapid aggregation of snow crystals that is also associated with strong vertical gradient of reflectivity in the layer. It is very likely that at the beginning of aggregation few crystals clump together and make a bigger, well oriented, and relatively dense aggregate, that produces pronounced Z_{DR} signature. Rapid aggregation leads to a wider size distribution of snowflakes and, as a result, to lower ρ_{hv} . This tendency, however, is offset by a decrease in snow density as it further aggregates and falls. Low-density snowflakes produce lower Z_{DR} and higher ρ_{hv} regardless of their shape and orientation.

At the ranges below 30 - 35 km from the radar, the aggregation at higher levels is weaker, vertical gradient of Z is smaller, and Z_{DR} and ρ_{hv} signatures are less pronounced. The aggregation, however, becomes more intense at lower levels where really large snow aggregates are likely generated. This is consistent with higher Z , very low Z_{DR} and K_{DP} , and high ρ_{hv} in the region between 0 and 40 km in range and 0 and 2 km in height (Fig. 9).

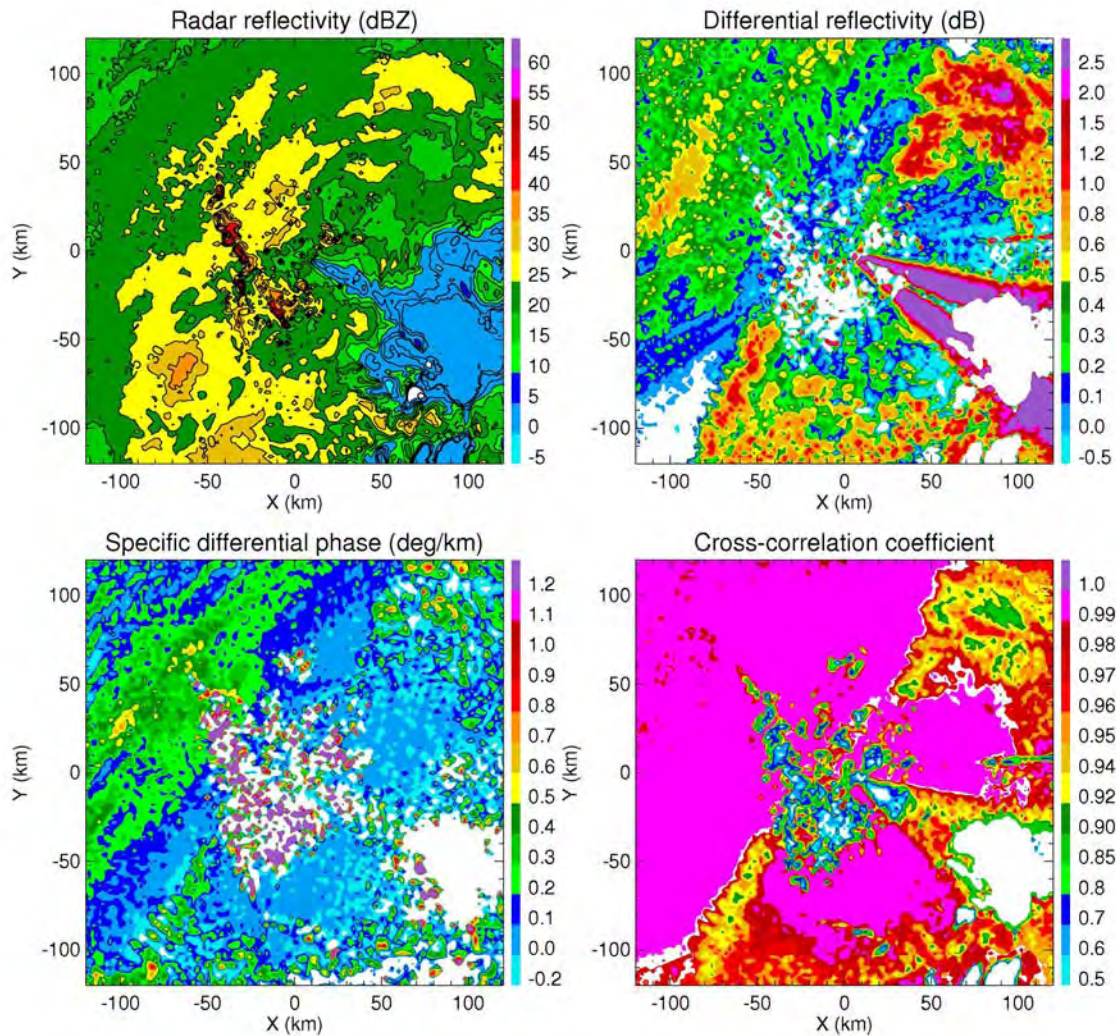


Fig. 8. Composite PPI plot of Z , Z_{DR} , K_{DP} , and ρ_{hV} at elevation 0.4° measured by the C-band polarimetric radar in mixed-phase precipitation on December 23, 2004 in the Toronto area in Canada. A sector in E-SE direction is affected by severe beam blockage. All three polarimetric variables clearly indicate the location of the rain / snow transition line, whereas reflectivity is not informative at all.

Monitoring aggregation processes in the frozen part of clouds is very important in evaluation of icing potential. Generally, an excessive aggregation inhibits icing, whereas riming favors it.

References

Giangrande, S.E., A.V. Ryzhkov, and J. Krause, 2005: Automatic detection of the melting layer with a polarimetric prototype of the WSR-88D radar. Preprints, 32nd Conference on Radar Meteorology., CD-ROM, 11R.2

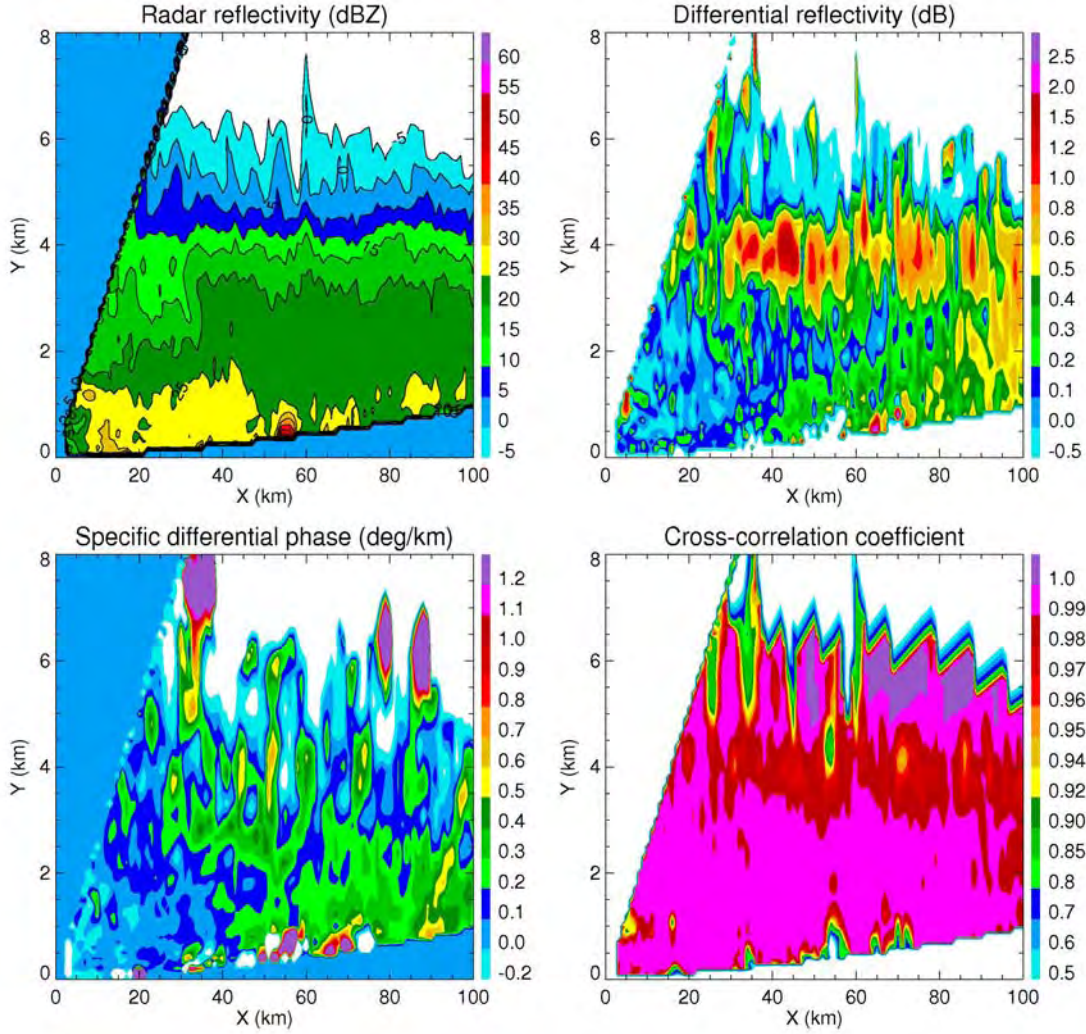


Fig. 9. Composite RHI plot of Z , Z_{DR} , K_{DP} , and ρ_{hv} at azimuth 310° measured by the C-band polarimetric radar in mixed-phase precipitation on December 23, 2004 in the Toronto area in Canada. The layer between 3.5 and 4.5 km is marked by high Z_{DR} and low ρ_{hv} indicative of rapid aggregation of snow crystals.

Edward A. Brandes¹, Kyoko Ikeda¹, Kimberly L. Elmore²,
Alexander V. Ryzhkov², and Terry J. Schuur²

¹National Center for Atmospheric Research

²Cooperative Institute for Mesoscale Studies, University of Oklahoma
and
National Severe Storms Laboratory

1. INTRODUCTION

Plans are proceeding to upgrade the national network of WSR-88Ds for polarimetric measurements. The radars will transmit electromagnetic energy at 45° (slant) polarization and receive returned signals at horizontal and vertical polarization. Because hydrometeors are not spherical, their radar backscattering cross sections are not the same for the two polarizations. Signal properties change continuously as the radar waves propagate yielding information that can be used to determine hydrometeor type (rain, snow, or mixed-phase), size, shape, and orientation. The added measurements of differential reflectivity, differential propagation phase, and correlation coefficient provide far more information regarding scatterers than is obtained from radar reflectivity alone. The measurements readily discriminate among ground targets, biological scatterers (insects and birds), and precipitation. Consistency among the measurements can be used to verify radar hardware calibration.

Demonstrated capabilities with polarimetric radar include improved rain-snow discrimination, hail detection, estimation of heavy rainfall rates, and freezing-level designation. Other benefits, likely to be developed long term, are improved quantification of winter (frozen) precipitation, detection of some icing conditions (especially situations involving embedded convection), estimation of precipitation-impacted visibility, detection of lightning precursors, and improved microphysical parameterization in numerical forecast models. Importantly, polarimetric measurements should also be useful for eliminating regions of the atmosphere where particular hazards are not likely. The net result will be better detection and quantification of weather hazards. Here we describe the polarimetric measurements and summarize potential benefits for aviation.

*Corresponding author address: Dr. Edward A. Brandes, National Center for Atmospheric Research, P.O. Box 3000, Boulder, CO, 80307; e-mail: brandes@ncar.ucar.edu

2. POLARIMETRIC MEASUREMENTS

The radar reflectivity factor Z at horizontal H and vertical polarization V for a unit volume can be expressed as

$$Z_{H,V} = \frac{\lambda^4}{\pi^5 |K_w|^2} \int_0^{D_{\max}} \sigma_{H,V}(D) N(D) dD,$$

where λ is the radar wavelength (mm), K_w is the dielectric factor for water, $\sigma_{H,V}(D)$ are the particle radar backscattering cross sections at horizontal and vertical polarization (mm^2), $N(D)$ is the particle distribution ($\text{mm}^{-1} \text{m}^{-3}$), and D is the particle equivalent volume diameter (mm). Reflectivity is generally computed in units of $\text{mm}^6 \text{m}^{-3}$ but expressed in dBZ ($10 \times \log Z_H$).

Differential reflectivity (Z_{DR} , in dB) is defined as

$$Z_{DR} = 10 \times \log(Z_H / Z_V)$$

with Z_H and Z_V in linear units. Differential reflectivity is positive (negative) for particles whose major axes are close to horizontal (vertical) in the mean. Raindrops tend to flatten and orient themselves with their major axes close to horizontal, giving Z_{DR} values typically between 0.3 to 3 dB. Hailstones tend to tumble as they fall creating a random distribution of orientations; Z_H and Z_V are similar in magnitude causing Z_{DR} to be small (< 0.5 dB). Dry snow aggregates tend to be more spherical than raindrops and have a lower dielectric constant. Consequently, Z_{DR} for snow tends to be small (< 1 dB). Z_{DR} for pristine ice crystals is typically larger than that for aggregates and may be 2 dB or more.

Another useful parameter is the correlation coefficient ρ_{HV} between horizontally and vertically polarized returns. This parameter is sensitive to the distribution of particle axis ratios, particularly for partly-melted hydrometeors and mixtures of hydrometeor types. Theoretical values are ~ 0.99 for raindrops, ice crystals, and dry aggregates. For hail and melting aggregates ρ_{HV} is typically less than 0.95.

The above parameters are derived from power measurements that depend upon

backscattering properties of illuminated particles. Radar waves are also subject to propagation effects such as attenuation and phase shifts. The differential phase shift Φ_{DP} between horizontally and vertically propagating polarized waves at a distance r is given by

$$\Phi_{DP}(r) = \Phi_0 + \delta(r) + \int_0^r K_{DP}(r) dr ,$$

where Φ_0 is the radar hardware offset between signals at the two polarizations, $\delta(r)$ is the backscatter differential phase shift, and K_{DP} is the two-way specific differential phase due to propagation. For an anisotropic medium like rain or pristine ice crystals, propagation constants for horizontally and vertically polarized waves differ.

Horizontally polarized waves “see” a larger particle cross-section and propagate more slowly than vertically polarized waves. Signals returned to the receiver for the two polarizations exhibit different accumulative phase (time) shifts depending on hydrometeor size, shape, orientation, quantity, and distance from the radar. In the absence of backscatter phase shifts, Φ_{DP} increases monotonically with range. Hail that tumbles or is near spherical in shape makes little contribution to K_{DP} . Large oriented hail will have little impact if it is dry because of its smaller dielectric constant. However, large wetted oriented hail and aggregates in the Mie scattering region can produce a backscatter differential phase shift that is manifest as a temporary decrease in Φ_{DP} .

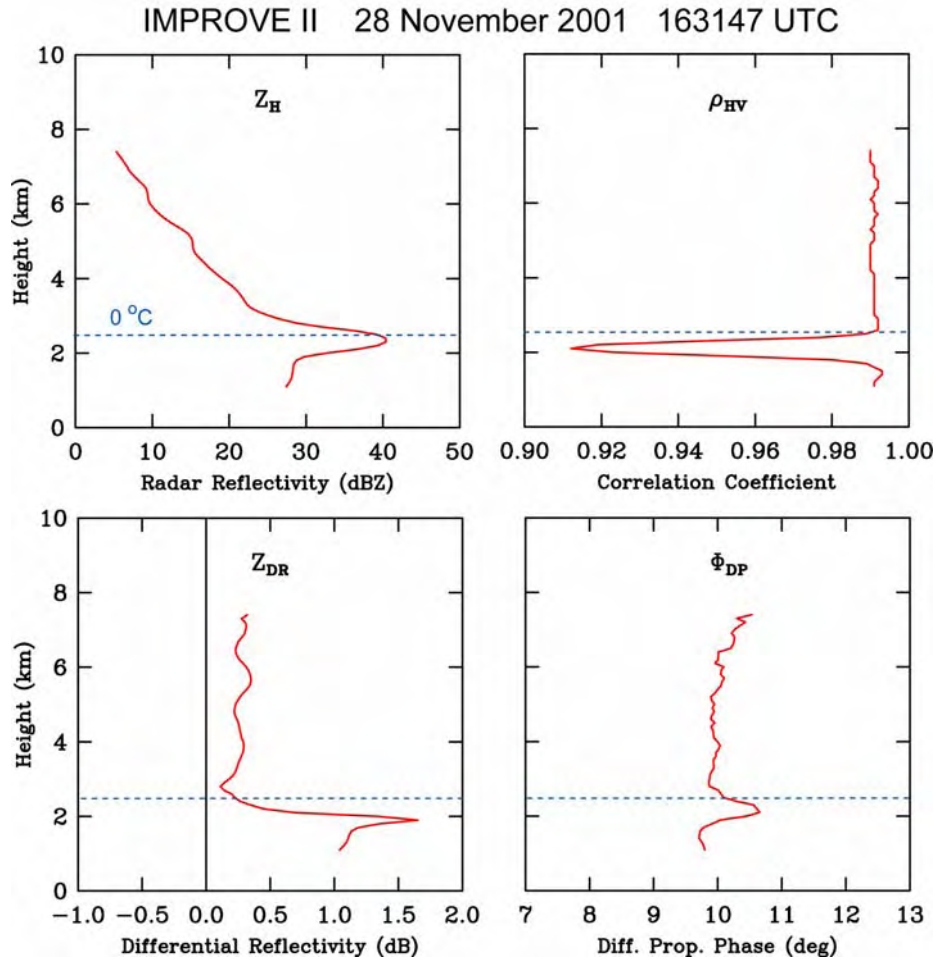


Fig. 1: Vertical profiles of polarimetric measurements constructed from vertical cross-sections. The freezing level is indicated by a horizontal line. Heights are above mean sea level.

Many properties of polarimetric measurements are exemplified by vertical profiles that pass through the melting layer (Fig. 1). The radar reflectivity bright band between 1.8 and 3 km responds to increased snowflake aggregation as temperatures warm to 0°C and to changes in dielectric factor as the hydrometeors melt. High reflectivity is also a sign of large particles. The layer of mixed-phase precipitation is characterized by a sharp decrease in ρ_{HV} as the distribution of particle shapes and types broadens. Correlation coefficients in the surface rain layer and upper snow layer are uniformly high. Differential reflectivity is relatively low in the snow layer and high in the rain layer. This observation is the foundation of rain-snow discrimination. The spike in Z_{DR} at ~2 km is a consequence of the melting process. The trace for Φ_{DP} shows a temporary increase due to the presence of Mie scatterers in the melting layer

and the monotonic increase, in this case with height, as the signals propagate. For additional discussion of these measurements and the signatures for various hydrometeor types readers should consult Doviak and Zrnić (1993).

Z_H and Z_{DR} measurement pairs for rain and snow are compared in Fig. 2. For rain Z_H and Z_{DR} are positively correlated. High reflectivity normally associates with high rain rates and larger, more flattened drops. Z_H and Z_{DR} are usually negatively correlated for snow. Radar returns from light frozen precipitation often exhibit characteristics of dense pristine hydrometeors with elongated horizontal axes, whereas heavy snow rates typically involve low density aggregates of pristine forms with shapes that are less flattened.

The distribution of Z_H and Z_{DR} measurement pairs in a hail-producing thunderstorm is shown in Fig. 3. The large size of the hail (¼ in) causes the reflectivity to be high, but the random hail

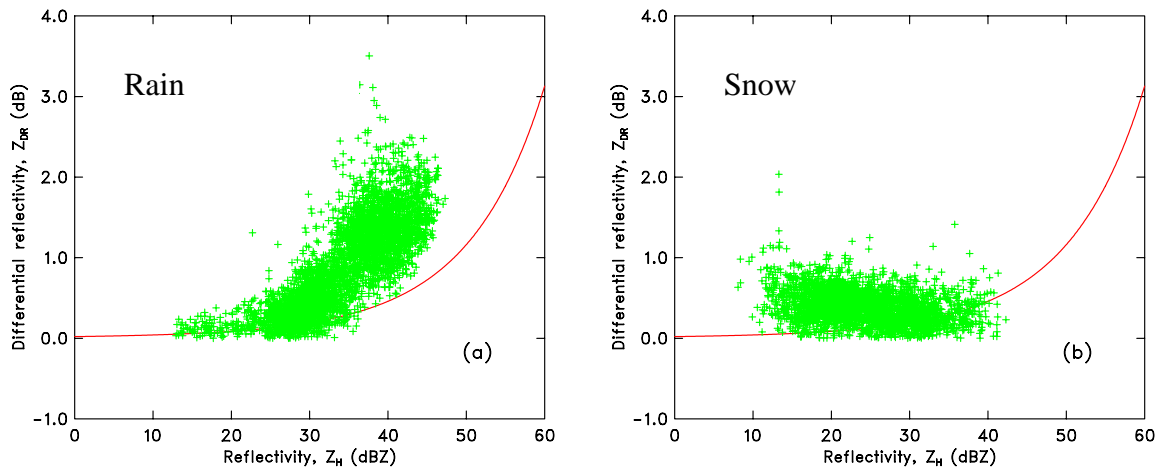


Fig. 2: Z_H and Z_{DR} measurements for freezing rain and snow regions in a storm that occurred in Oklahoma on 5 January 2005 (1311 UTC).

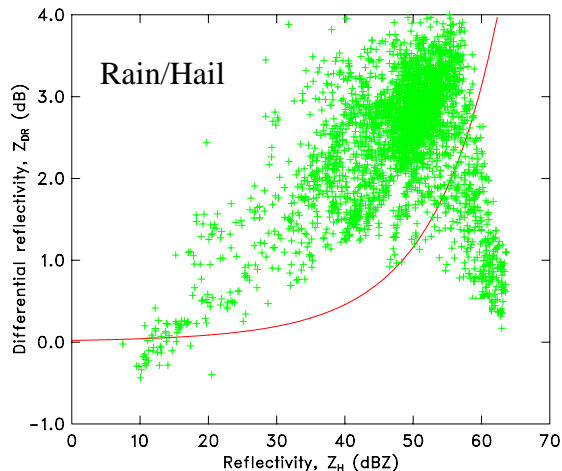


Fig. 3: As in Fig. 2, except for a hailstorm in Oklahoma on 13 June 2002 (0055 UTC).

orientation reduces the differential reflectivity, creating a negative correlation between Z_H and Z_{DR} at high reflectivity. Data points with $Z_H > 60$ dBZ and $Z_{DR} < -2$ dB are clearly contaminated by hail. Further, their separation from data points associated with heavy rain ($Z_H = 50$ dBZ and $Z_{DR} = 3$ dB) is an indication of hail size.

3. IMPACTS ON DATA QUALITY

Polarimetric measurements allow consistency checks among variables that can be used to verify the hardware calibration. For example, the differential propagation phase can be computed from the Z_H and Z_{DR} measurements (Vivekanandan et al. 2003). Comparison with the radar-measured value can then be used to validate the radar calibration for reflectivity, assuming Z_{DR} (a difference quantity) is known. Experience suggests bias in Z_H can be reduced to about 0.5 dB by this procedure.

Insects have a large Z_{DR} signature (often 5 dB and more) but a ρ_{HV} of about 0.8 (Zrnić and Ryzhkov 1998). The number density of insects is usually small so that their reflectivity is low. Differential phase is usually small and, if the insects are large, may exhibit a backscatter component δ . Migrating birds are distinguished by low Z_H (< 20 dBZ), a Z_{DR} of 3–4 dB, and large δ (100° and more). An ability to detect and perhaps remove biological scatterers should lead to improvements in winds derived from velocity–azimuth displays (VADs) and radar-based precipitation estimates.

Scattering from ground targets causes large random differential phase shifts, reduces the correlation coefficient to 0.8 and less, and creates high spatial variance in Z_{DR} measurements. Consequently, additional pattern texture parameters are available for discriminating between precipitation and ground echoes.

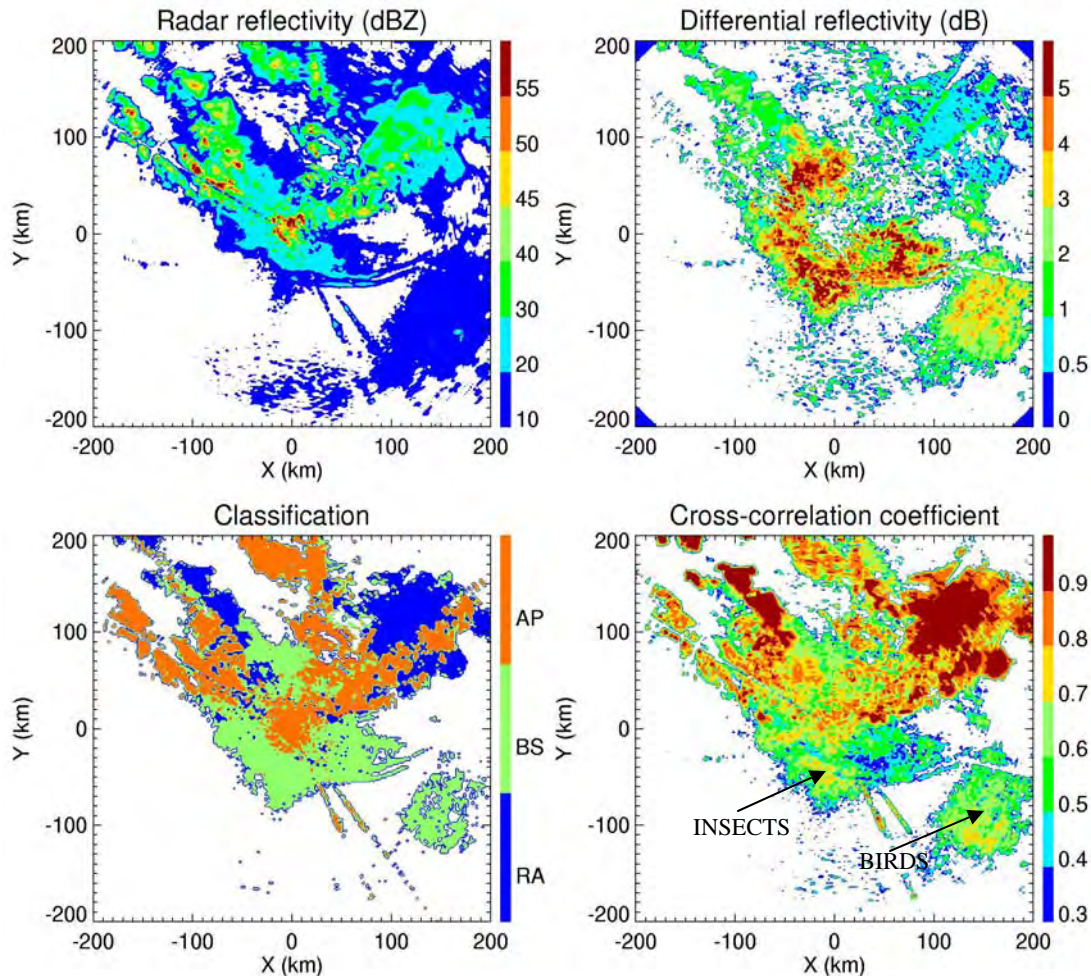


Fig. 4: An example of radar echo designations made with a version of the NSSL HCA. Classifications are made for ground clutter and anomalous propagation echoes (AP), biological scatterers (BS, insects and birds), and rain echoes (RA).

4. POTENTIAL NEW PRODUCTS

As suggested in Section 2, polarimetric measurements should lead to improved rain-snow discrimination and hail detection. As research progresses, there will be better quantification of frozen precipitation as well. An ability to retrieve raindrop-size distributions in precipitation (e.g., Brandes et al. 2004) is increasing the understanding of precipitation processes and will result in improved microphysics parameterization in numerical forecast models. The raindrop retrieval capability will support better estimates of precipitation-impacted visibility at airports than is currently available from radar reflectivity measurements alone.

An example of a Hydrometeor Classification Algorithm (HCA) product being developed at the National Severe Storms Laboratory is presented in Fig. 4. Radar echoes from precipitation (rain), ground targets, and biological scatterers are indicated. An example of a prototype research HCA under development at the National Center for Atmospheric Research is shown in Fig. 5.

Designations are made for several precipitation types, insects, ground clutter, and range folded echoes. An attempt is made to identify regions of potential icing conditions (super-cooled liquid water). Research suggests that icing hazards associated with large super-cooled drops is possible—provided the radar returns from drops dominate that of frozen particles that may be present.

Knowing the vertical distribution of radar measurements, e.g., Fig. 1, and the statistical relationship that exists between the height of melting layer signature extremes and the 0°C level, it is possible to estimate the freezing-level height with an accuracy of 100–200 m (Brandes and Ikeda 2004). Such information is needed by HCAs for discriminating between liquid and frozen precipitation types, can be used to nudge numerical forecasts in models that ingest observations, and aids in the isolation of precipitation layers with potential icing hazard. The power to designate precipitation as rain or drizzle when sub-freezing temperatures exist should reduce occurrences of this icing hazard.

22 September 1998: 1956 UTC

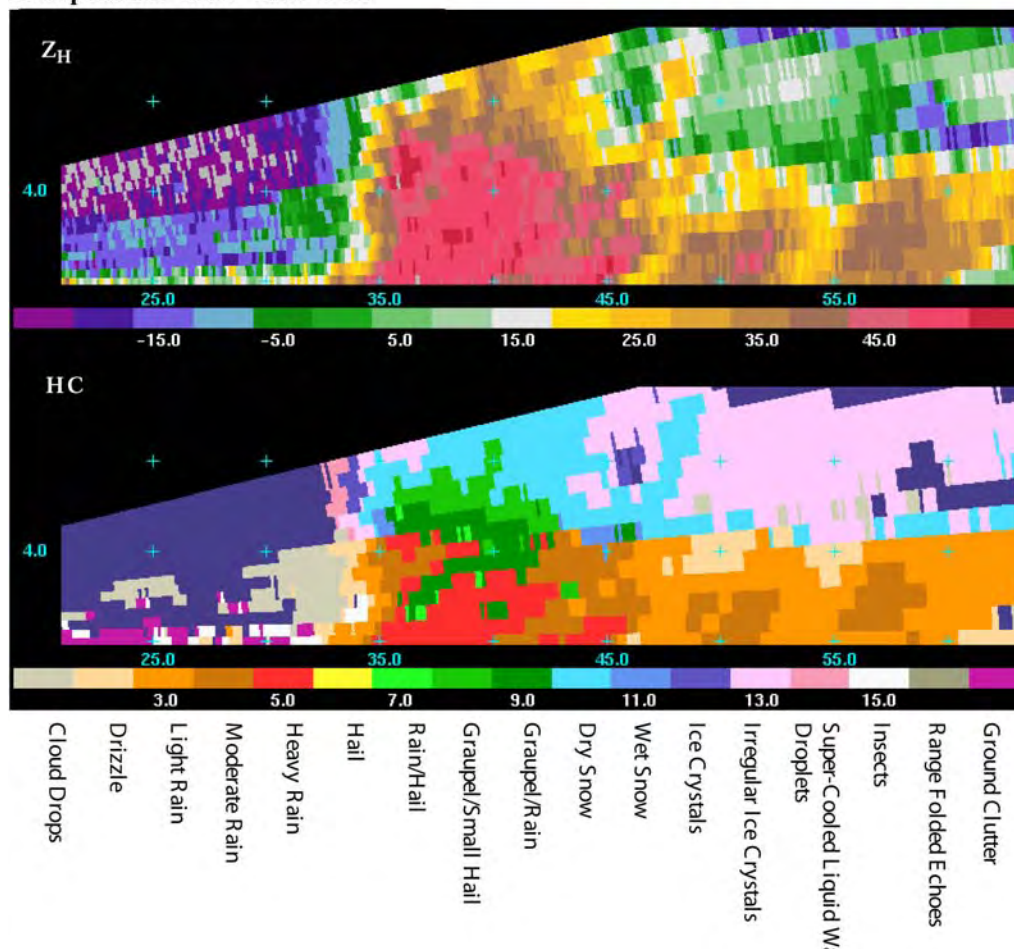


Fig. 5: Radar echo designations made with the NCAR HCA.

5. SUMMARY AND CONCLUSIONS

The impact of polarimetric measurements on aircraft operations and severe weather warning should rival the Doppler capability that became available with the installation of the WSR-88D network. New capabilities for the designation of potential icing hazards exist that simply aren't possible with radar reflectivity measurements alone. Existing radar-based algorithms being developed for the aviation community will benefit from an overall improvement in radar data quality. Other expected benefits include enhanced skill in detecting hail, tornadoes (Ryzhkov et al. 2005), some icing conditions, and rain-snow discrimination. The latter ability could help determine when deicing fluids are needed and the type required. A capacity to designate freezing levels and hydrometeor types should lead to improved numerical forecasts. The net effect will be improved safety and situation awareness.

References

- Brandes, E. A., and K. Ikeda, 2004: Freezing-level estimation with polarimetric radar. *J. Appl. Meteor.*, **43**, 1541–1553.
- Brandes, E. A., G. Zhang, and J. Vivekanandan, 2004: Drop size distribution retrieval with polarimetric radar: Model and application. *J. Appl. Meteor.*, **43**, 461–475.
- Doviak, R. J., and D. S. Zrnić, 1993: *Doppler Radar and Weather Observations*. Academic Press. 562 pp.
- Ryzhkov, A. V., T. J. Schuur, and D. W. Burgess, 2005: Polarimetric tornado detection. *J. Appl. Meteor.*, **44**, 557–570.
- Vivekanandan, J., G. Zhang, S. M. Ellis, D. Rajopadhyaya, and S. K. Avery, 2002: Radar reflectivity calibration using differential phase measurement. *Radio Sci.*, **38**, doi:1029/2002RS002676.
- Zrnić, D. S., and A. V. Ryzhkov, 1998: Observations of insects and birds with a polarimetric radar. *IEEE Trans. Geosci. Remote Sens.*, **36**, 661–668.

06.6.34.1 Further enhancements of the reflectivity QC procedure

The NSSL continues the identification and archive of events associated with radar reflectivity quality control. The QC events are used to test the effectiveness of QC applications to remove and/or mitigate the presence of non-meteorological radar returns. Specifically we attempt to identify and archive radar and other observational datasets for situations where non-meteorological returns would result in unrealistic portrayals of storm structure within the high-resolution national 3-D radar mosaic.

Events are identified and entered into the database in ‘real time’ and/or during individual case studies. When an event is identified, level-2 (base level) radar data is archived and the event classified into one (or more) of eight categories. Table 1 provides the categories and the number of case events archived for each classification. The number of events archived is not indicative of relative frequency of the individual categories. Rather NSSL scientists select cases based upon varying geography, season, and time of day as well as uniqueness. However, the most common and perhaps the most difficult QC issue is the presence of biological targets especially during the warm season. Biological targets can manifest themselves across several of the categories listed in Table 1.

Table 1. Categories and number of cases within the Quality Control archive.

Category	Number Events
Birds and Insects	4
Sea Clutter	36
Hardware Test Pattern	22
Chaff	1
AP/Ground Clutter	34
Sun Beam/Speckles	3
Isolated Storms	4
Shallow Precipitation	42

Figure 1 is an excerpt from the database depicting how QC events are documented as part of the archiving process. The radar, time and file locations are noted in addition to a subjective evaluation made (Good, Okay, and Poor) as to the initial performance of QC application for that particular event. The archived events are then used as an improvement baseline to test updated and new quality control techniques used in the creation of the 3D mosaic products and associated derivatives.

	A	B	C	D	E	F	G	H	I	J	K	L	M
1	RADAR	TIME STRING	RAW	BINARY	NIDS	GOOD	OKAY	POOR	Comments				
2	KFWS	19950419154948			ON MNT2/KCAE				Some ground clutter to S/SE mixed in with precip at far range				
3	KFWS	19950419155537			ON MNT2/KCAE				Clutter to north of radar and S/SE with precip at far range				
4	KTLX	20021019160754			ON MNT2/KCAE								
5	KAKQ	20030210071027			ON MNT2/KCAE				Is this meteorological - maybe shallow winter storm				
6	KIWA	20030212154140			ON MNT2/KCAE				Also in AP_GC category				
7	KYUX	20030213125114			ON MNT2/KCAE								
8	KIWA	20030318023019			ON MNT2/KCAE								
9	KTLX	20030515143456			ON MNT2/KCAE								
10	KIRX	20030520102054			ON MNT2/KCAE				far range precip plus ground clutter				
11	KTLX	20030520163914			ON MNT2/KCAE								
12	KTLX	20030611080651			ON MNT2/KCAE				blooms and precip at far range				
13	KTLX	20030611112443			ON MNT2/KCAE								
14	KTLX	20030613091330			ON MNT2/KCAE								
15	KEMX	20030924101321			ON MNT2/KCAE								
16	KFSX	20030924165409			ON MNT2/KCAE				white mountains to south east				
17	KTLX	20031113113759			ON MNT2/KCAE				bloom around radar				
18	KTLX	20031113125318			ON MNT2/KCAE				gc near radar all remaining echo is real				
19	KXXX	20040226143415			ON MNT2/KCAE				Shallow precip - snow??				
20	KXXX	20040412144532			ON MNT2/KCAE				Shallow precip				
21	KXXX	20040423150410			ON MNT2/KCAE				Precip far range - removes core echoes				
22	KXXX	20040423160343			ON MNT2/KCAE				Precip at very far range				

Figure 1 – Snapshot from QC archive spreadsheet with event information for the shallow precipitation category.

Figures 2a and 2b are example chaff ‘clouds’ originating from military ranges in western Arizona. The occurrence of chaff is frequently observed in nearly all regions where there exist military training facilities or ranges. Chaff is also observed offshore in the Gulf of Mexico and along the US east coast. Chaff, typically hairline fiberglass coated with aluminum, is often mistaken (by human and radar algorithms) as precipitating cloud and even storms. Chaff clouds have been observed to extend as high as 35 kft for many hours with reflectivities exceeding 50 dbz during initial discharge from a military aircraft. Given ability of chaff to mimic storms, chaff poses a significant problem for quality control. NSSL has been researching and testing the combination of radar and an effective cloud cover mask determined from multi spectral satellite data to identify the presence of chaff and remove it prior to being incorporated into the 3D mosaic. Real time implementation of the satellite effective cloud cover mask is currently being evaluated for the High-Resolution National 3-D Radar Mosaic.



Figure 2a Chaff clouds and streaks in western Arizona and southern Nevada. Note that large areas of reflectivities exceed 25 dbz with maximum reflectivities of great than 35dbz.

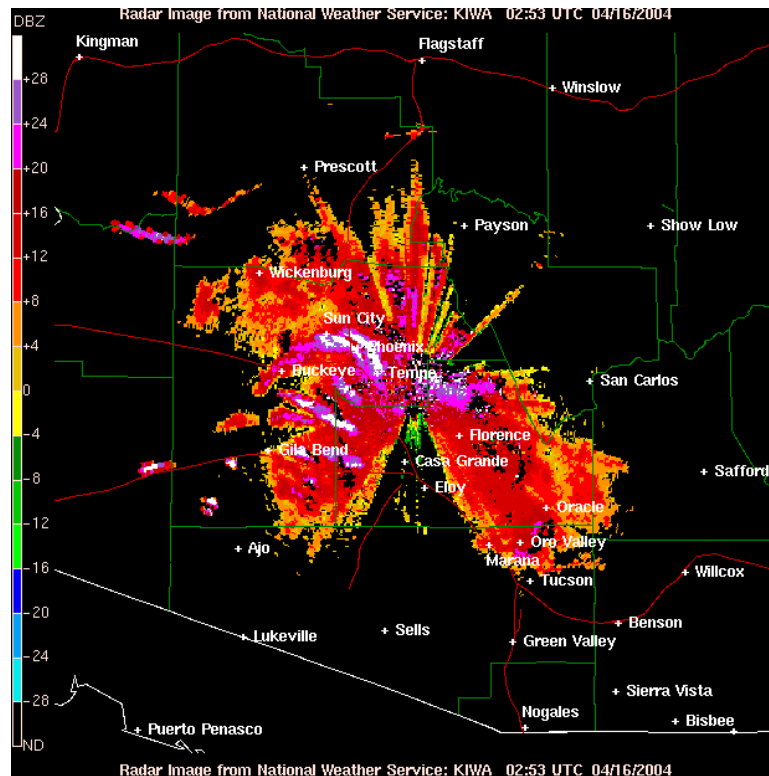


Figure 2b Chaff clouds and streaks in central Arizona combined with ground clutter around the KIWA radar.

Radar reflectivity returns from birds and insects pose a significant and frequent problem during the warm season and during North America bird migrations. Figure 3a shows an example of radar reflectivity ‘bloom’ as a result of a boundary layer composed of insects and birds. The radar reflectivity blooms are most apparent when the radar is operating in clear air mode (VCP31 or 32). Figure 3b shows the extent of a bloom in the Midwest as a result of bird migrations extending northward. A simplistic approach was initially implemented with the national 3-D mosaic to remove any radars operating in VCP 31 and 32 from being included into the national 3-D mosaic. The technique was further refined to only remove radars operating VCP 31 or 32 when the surface temperature near the radar was above 40F based upon RUC analysis. The reasoning behind utilizing a surface temperature threshold is due to radars being placed in clear air mode (VCP 31 or 32) during winter precipitation events to improve the sensitive of the radar to observe snow and other frozen precipitation. However, additional logic is required to improve the effectiveness of removing insects and birds, prior to national implementation of dual polarization, especially during the seasonal transitions when winter precipitation and bird migrations coincide. Additional logic is under consideration and development includes combining surface observations and satellite imagery along with texturing techniques (as per the REC) for multi sensor approach for removing QC

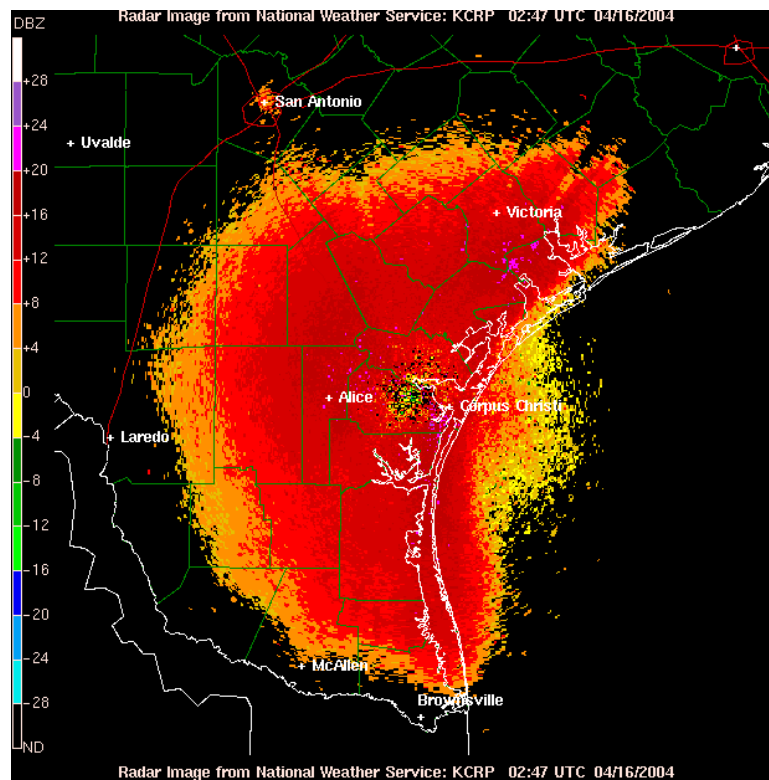


Figure 3a A radar reflectivity 'bloom' as a result of nocturnal bird migrations during the early spring.

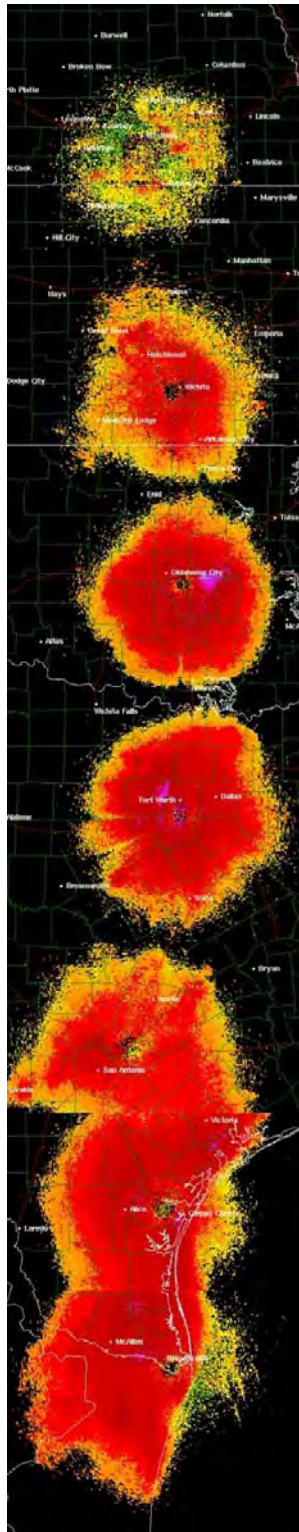


Figure 3b Radar reflectivity ‘blooms’ extending through the Midwest as a result of nocturnal bird migrations during the early spring.

Figures 4a-c depicts the examples of the daily occurrence of sunbeams, spikes and speckles. A filtering technique was developed to specifically remove the spikes and speckles or similar feature. The sunbeam or spike filtering technique is fairly effective with exception of situations when the beam spikes are abnormally wide or discontinuous. Speckles are isolated pixels of reflectivity, which may be a result of number of factors including radar interference, towers, mountaintops, birds, etc. A 9x9 noise filter was developed to address speckles from a single point to small grouping. The noise filter technique is effective but is often too aggressive on the edges of meteorological features. Further testing and refinement is currently underway to improve both filtering techniques.

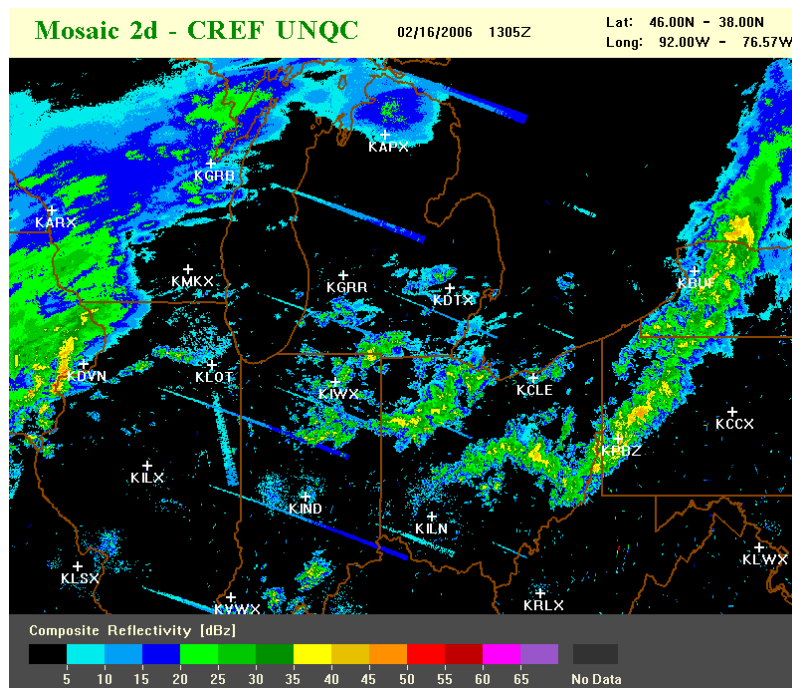


Figure 4a An example composite reflectivity mosaic field showing sunbeam echoes from various radars around sunrise time.

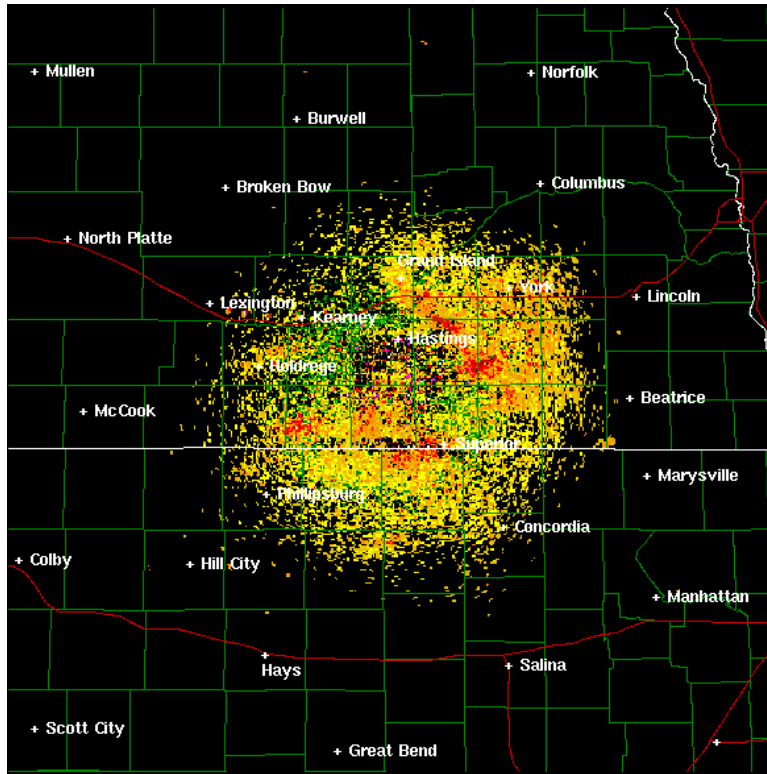


Figure 4b Example radar reflectivity field with speckles.

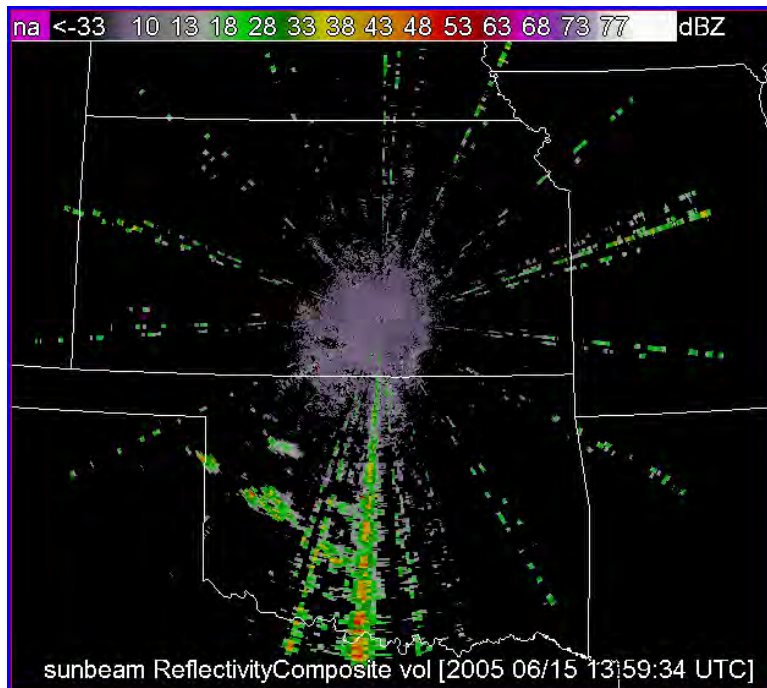


Figure 4c Example radar reflectivity field with spikes.

06.6.34.2 Continued development of a gap-filling scheme using vertical profiles of reflectivity.

The activities during this quarter include studies of vertical profiles of reflectivity (VPRs) for the Hurricane Isabel. Reflectivity observations from five radars in North Carolina are analyzed. The analysis results from the KMHX (Morehead City) are presented here.

Figure 5 shows a time series of the composite reflectivity observed by KMHX radar from 02Z to 22Z on Sept. 18, 2003. The eye of the hurricane made the landfall between 16Z and 18Z (Figs. 5f and 5g). The maximum reflectivity was less than 50dBZ during the time period indicating that there was little deep convection present. The time series of vertical cross section (the “a” column in Fig. 6) confirmed the non-deep convective nature of the system. For the majority of the time, the echo top (of 18dBZ or higher) was below 8 km (MSL). The reflectivity was mostly below 50dBZ even within the most intensive rain bands. The precipitation type fields (not shown) also indicated very few convective precipitation pixels. Hence only the hourly mean stratiform VPRs are presented herein.

The hourly mean stratiform VPRs are shown in the “c” column of Fig. 6. Between 06-07Z, the VPR shows a clear maximum at the height of ~4.3km. This is consistent with the maximum reflectivity layer in the corresponding cross section image (Fig. 6-a1). The maximum reflectivity layer shows a typical bright band feature. The sounding observations at the 06Z (Fig. 7a) confirms that the maximum reflectivity layer is consistent in height with the 0°C level. Below the bright band, the reflectivity decreases as the height decreases. Since the atmosphere below the freezing level is relatively dry (Fig. 7a), part of the reflectivity decrease was probably due to the evaporation of the hydrometeors. As the hurricane moved inland, the reflectivity at the low levels continued to grow (Figs. 6-c2, c3, c4, c5, c6, and c7). This is likely a result of heavy rainfall associated with the moist marine air mass moving near the radar (recall that the VPRs are derived in the annular region of 20-80km range from the radar, see the 3rd quarterly report in FY05 for task 05.6.34.2). Additionally, as the marine air mass moved inland, the bright band layer became less pronounced in the vertical cross sections (Fig. 6-a1 vs. Figs. 6-a2, a3, etc). This is due to the fact that the marine air mass is much warmer than the land air mass and a strong temperature gradient is located along the coastal line at the 06Z (Fig. 8). The vertical cross-sections bisects through the two rain bands (Fig. 9), one over the land (“A” in Fig. 9b) and one over the ocean (“B”, Fig. 9d) showed very different vertical structure. A bright band layer is clearly present in the rain band “A” (Fig. 9a) but not in the rain band “B” (Fig. 9c).

A majority of the hourly mean VPRs (see Figure 6) have small standard deviations indicating that the vertical structure of the storms have common characteristics in space and time. However, the VPR between 14 and 15Z shows a large variation below 5km. Further investigations will be carried out on the cause of the large variations of the VPR during this time period.

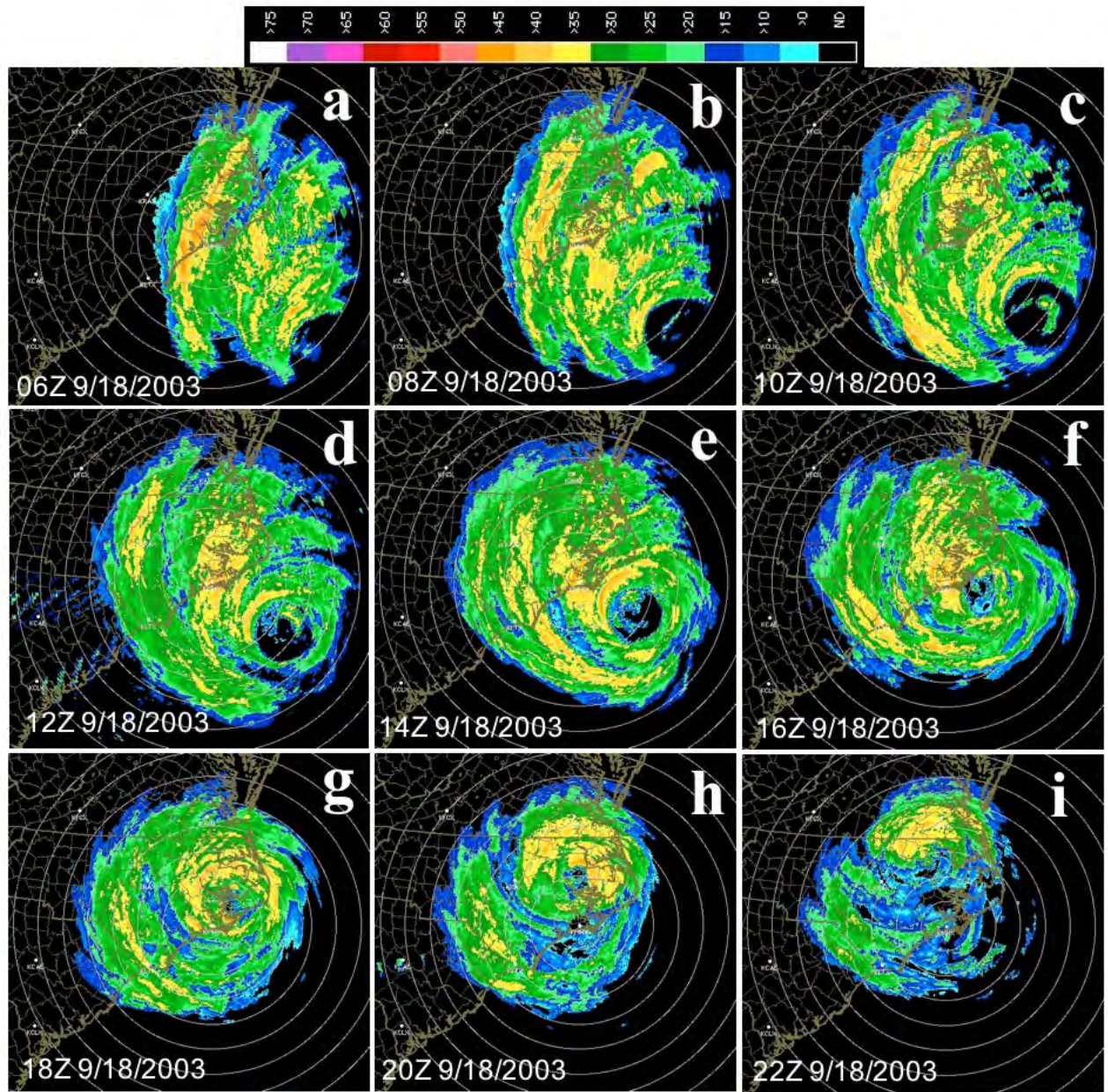


Fig.5 Composite reflectivities observed by KMHX radar from 02Z to 22Z on Sept.18, 2003.

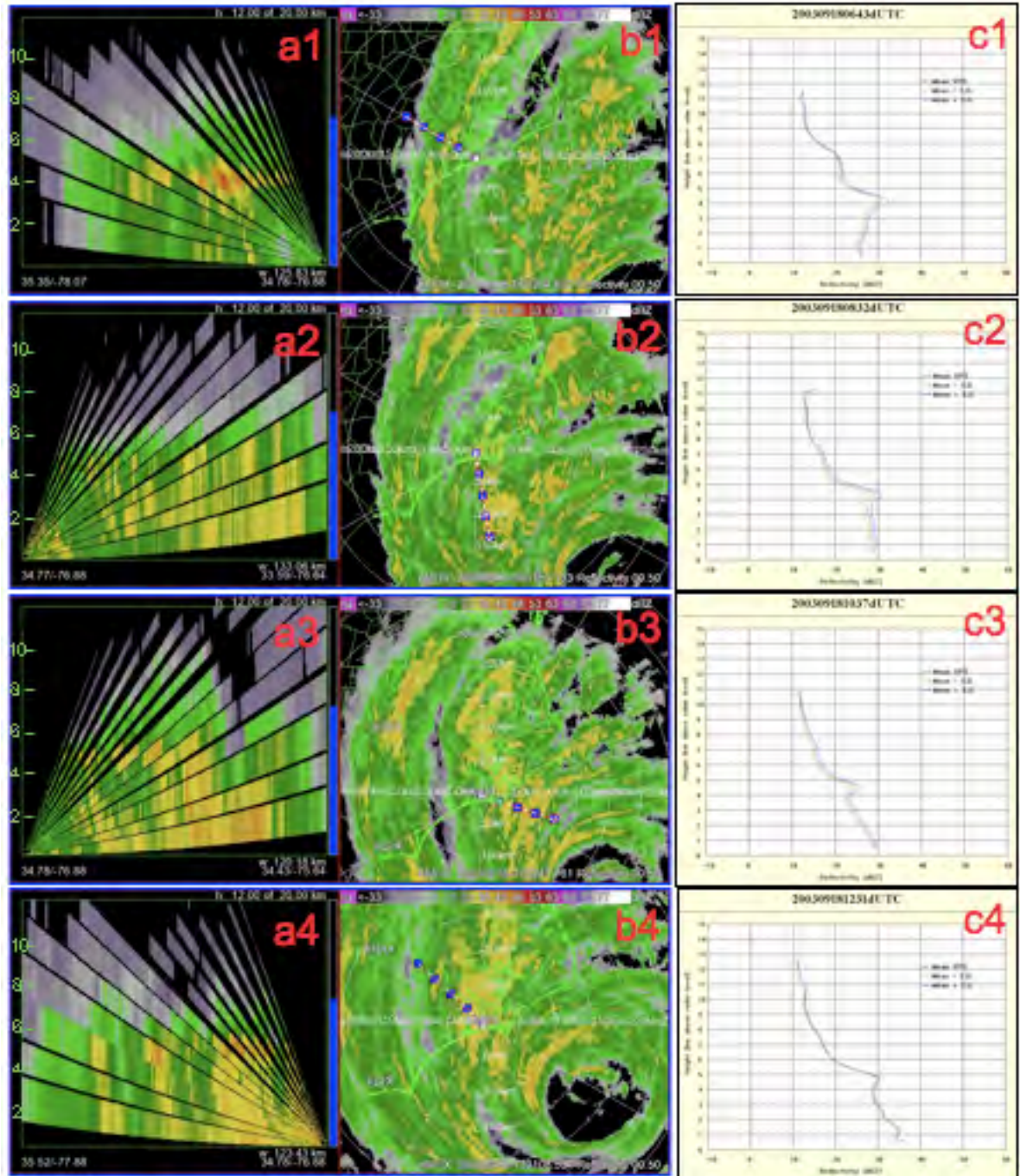


Fig.6 Vertical cross sections of reflectivity (left, or, “a”, column), composite reflectivity (middle, or, “b”, column) and hourly mean VPRs (right, or, “c”, column) from KMHX radar observations from 02Z to 22Z on Sept.18, 2003. The lines that connect the blue squares in “b” columns show locations where the vertical cross sections were taken. The time shows in the VPR plots indicate the time in the middle of the hour.

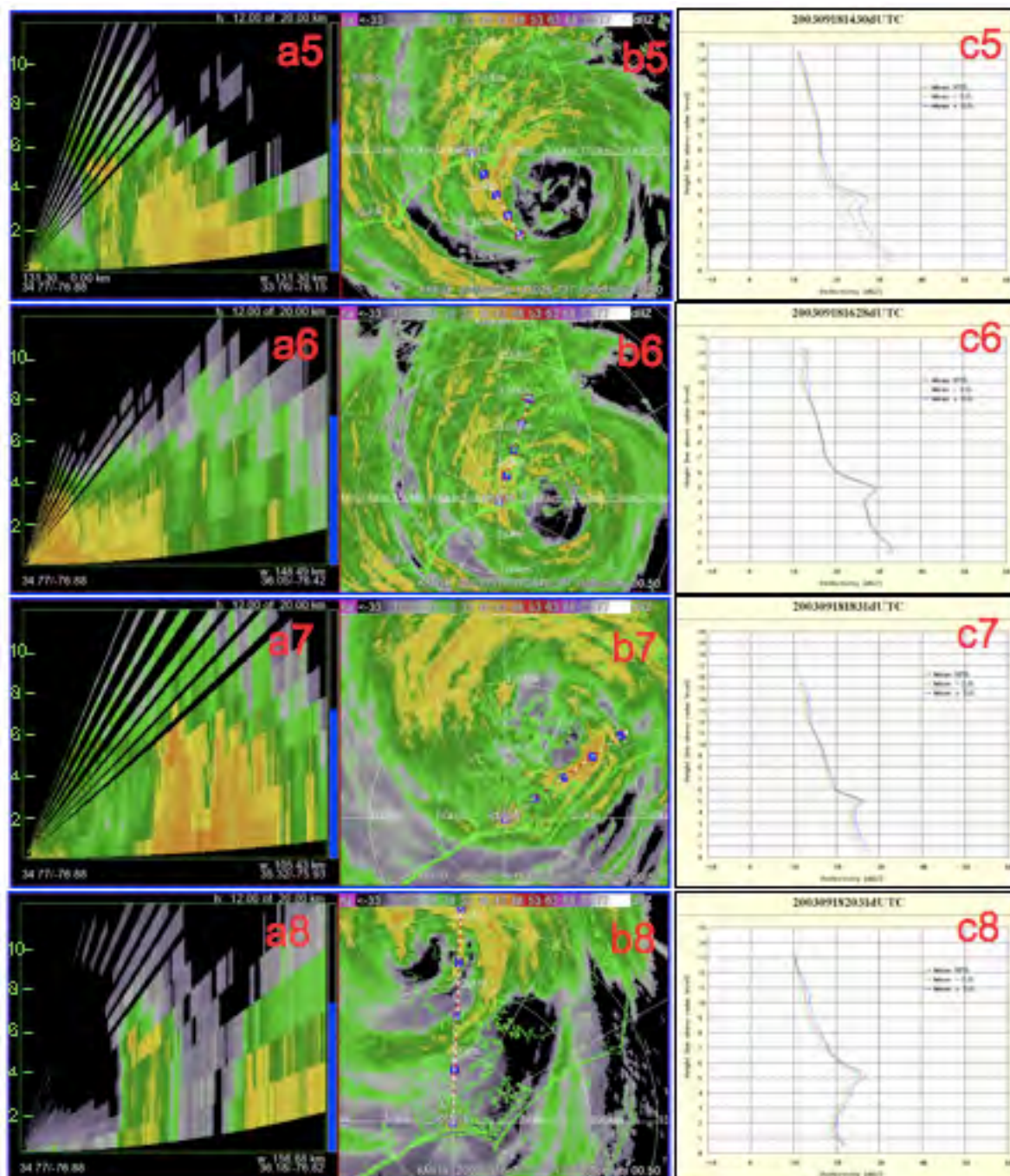


Fig. 6 Continued.

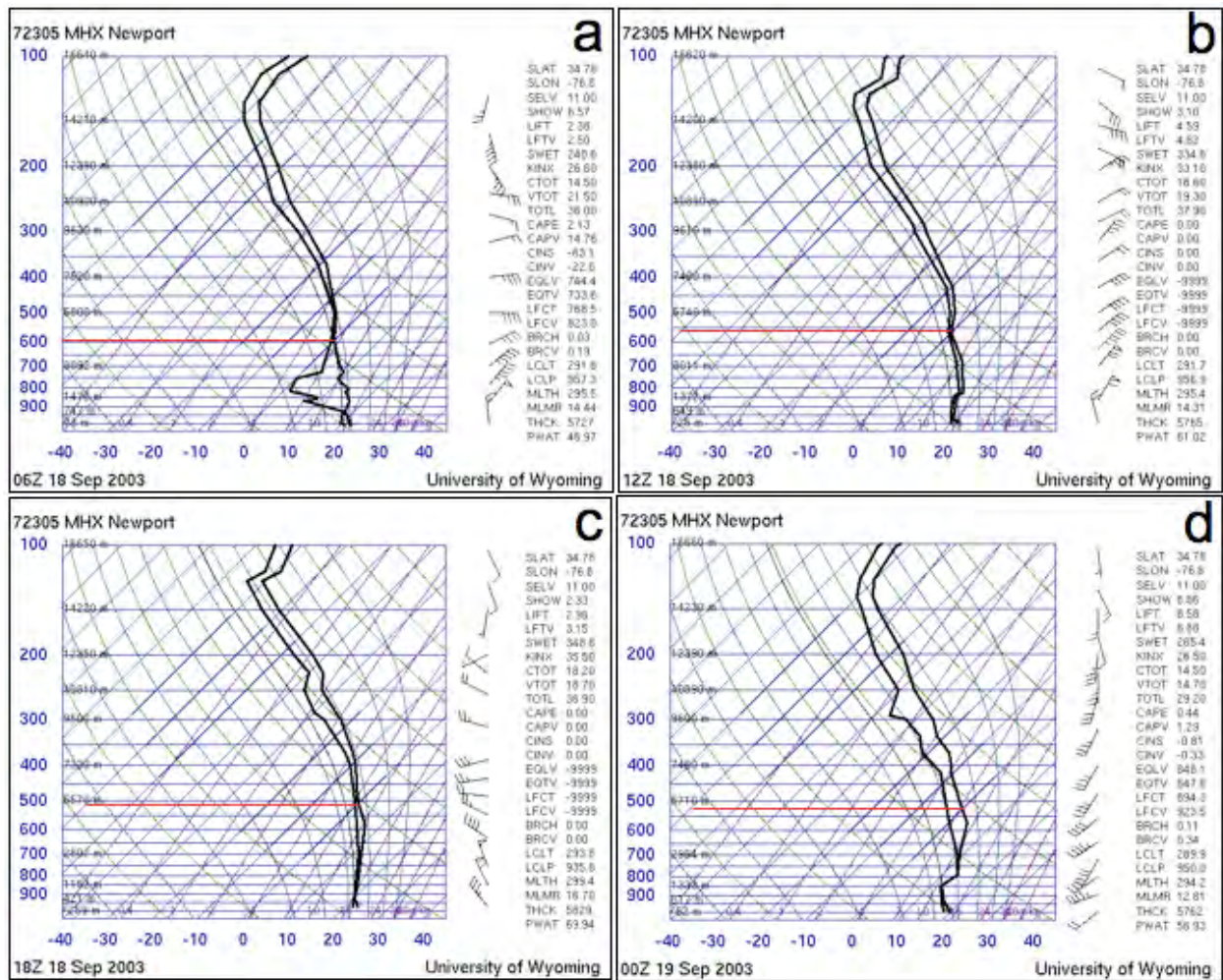


Fig.7 Skew-T plots of the soundings at the MHX (Newport, NC) station at 06Z (a), 12Z (b), 18Z (c), on Sept. 18 and 00Z on Sept. 19, 2003. The red lines indicate the 0°C height.

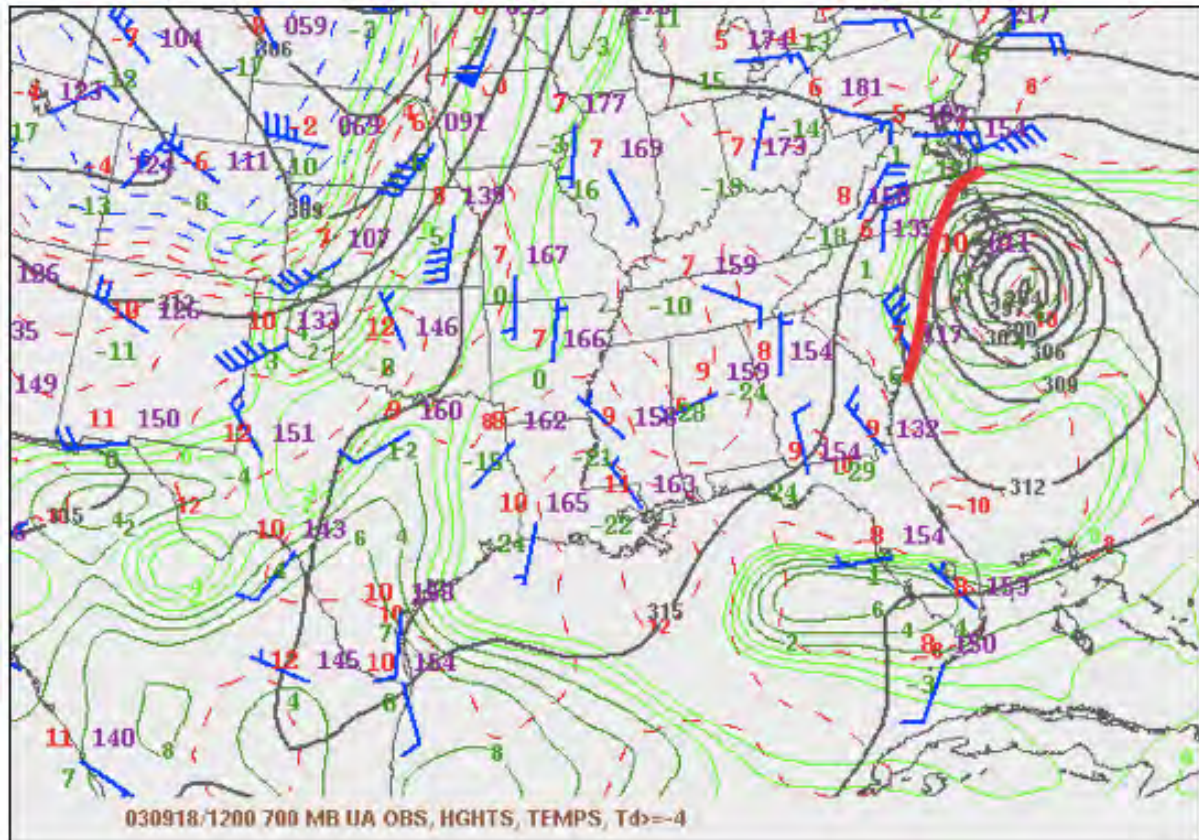


Fig.8 700mb weather map at 12:00 UTC on Sept. 18, 2003. The bold red line indicates the rough location of a warm front.

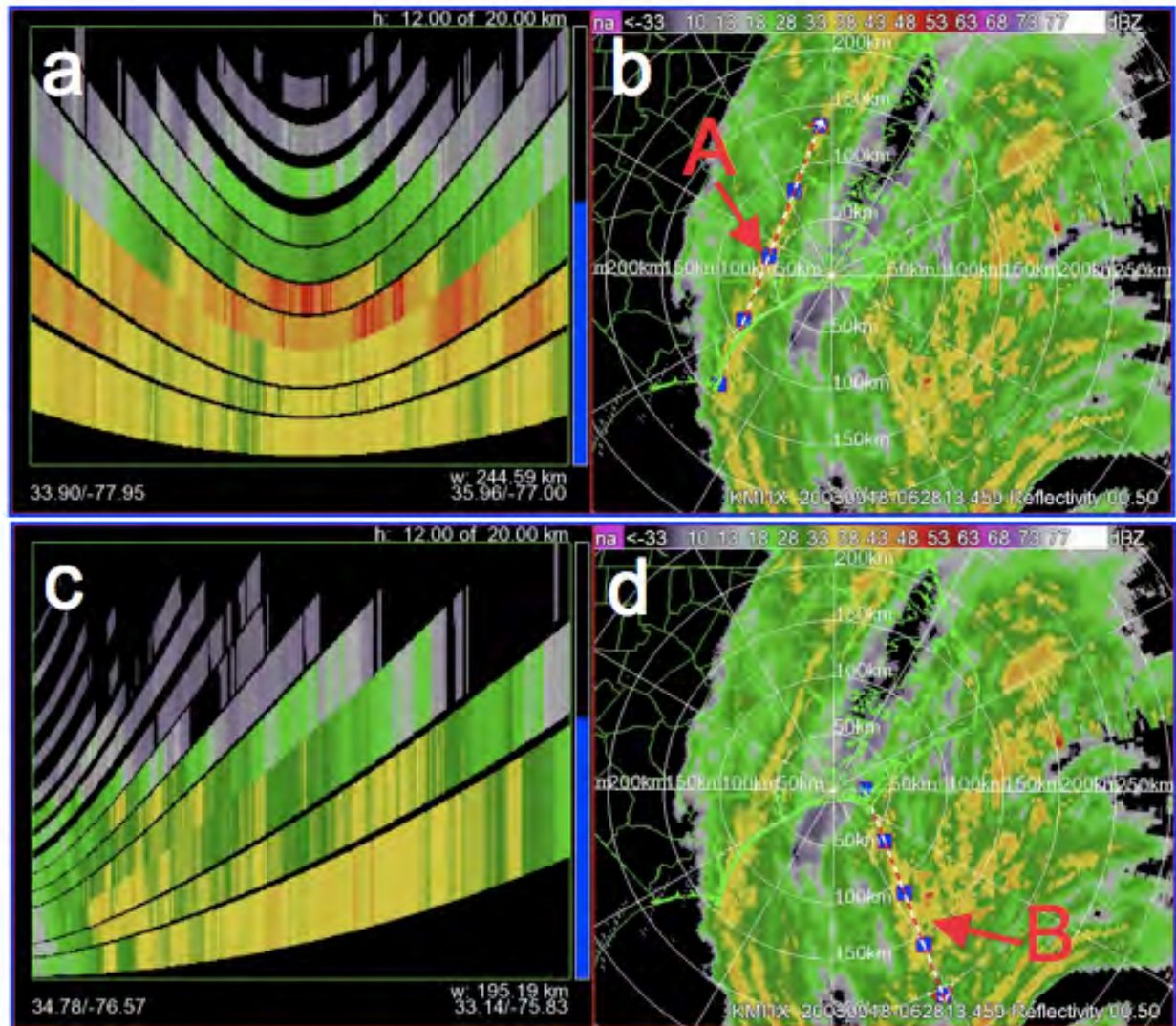


Fig.9 Vertical cross-sections (a, c) and composite reflectivities (b, d) at 06:28UTC on Sept.18, 2003.

06.6.34.3 Develop evaluation methods for the gap-filling technique using vertical profiles of reflectivity.

The gap-filling procedure is carried out within the single radar Cartesian (SRC) grid. The procedure includes the following steps:

- 1) Computing hourly mean VPRs from quality controlled reflectivity data in the native radar coordinates (i.e., spherical coordinates);
- 2) Remapping/analyzing the quality controlled reflectivity data from the native coordinates onto a Cartesian grid (i.e., the SRC grid);
- 3) Filling in data voids below the lowest radar beams in the SRC using the hourly mean VPRs.

Note that the VPRs are calculated in the native coordinates to retain the high-resolution information in the raw radar observations.

To evaluate the gap-filled SRC grid, we propose to use an independent SRC grid from a nearby radar. Since the SRC grids from different radars are fully aligned when they are overlapping (see the 3rd quarterly report in FY05 for task 05.6.35.1), an inter-comparison between overlapping SRC grid cells is relatively straightforward and various statistics can be obtained. The evaluation of the VPR and gap-filling schemes will be carried out in the next quarter.

06.6.34.4 Continued evaluation and improvement of the multi-radar synchronization technique.

(This task starts in the 2nd quarter.)

06.6.34.5 Collect Canadian radar data and develop strategies for integration of Canadian radar data into the national 3D mosaic.

(This task starts in the 2nd quarter.)

05.6.34.6 Creation and maintenance of user-defined archival process for the CONUS 3-D and 2-D severe weather products.

The activities for this quarter include continued support of the 3D CONUS reflectivity mosaic grid and the related 2D products to several other PDTs.

06.6.35.1 Continue optimization of the single radar 3-D Cartesian grids.

During this quarter, the code for the single radar Cartesian (SRC) grid has been further optimized. The code was implemented in real-time to generate single radar analysis grid and the associated products from ~140 radars in the CONUS. The products include the reflectivity analysis on a 3-D Cartesian grid and a suite of 2-D products on a regular $1^\circ \times 1\text{km}$ polar grid. The 2-D products include base reflectivity (with and without the quality control), radial velocity (both the raw and the dealiased), composite reflectivity (before and after the QC), and the height associated with the composite reflectivity, etc. A complete list of the 2-D polar products can be found in Table 2. The 3-D Cartesian grid has a size of $601\text{km} \times 601\text{km}$ for inland radars and $921\text{km} \times 921\text{km}$ for coastal and the United States border radars (Figure 10). All Cartesian grids are in the cylindrical equidistant map projection with a horizontal resolution of $0.01^\circ \times 0.01^\circ$ and have 31 levels in the vertical ranging from 500m to 18km above MSL (Table 3).

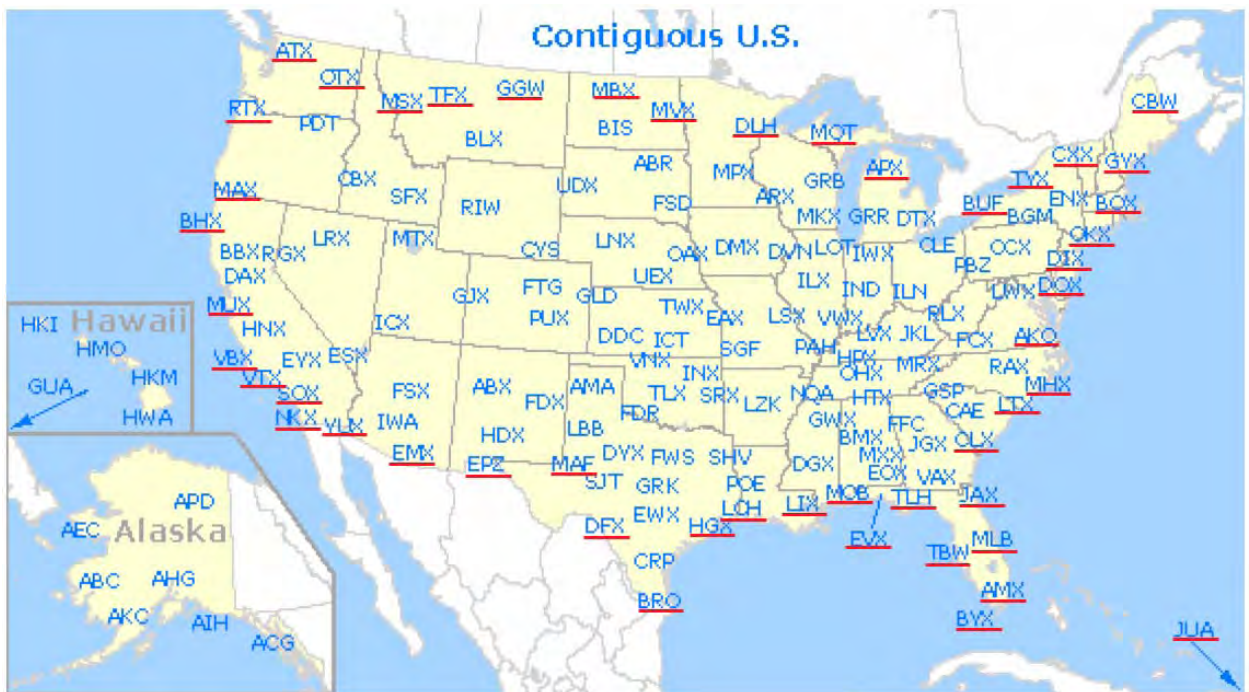


Fig. 10 A map of the WSR-88D network. The radar sites with red underlines have the SRC grid of $921\text{km} \times 921\text{km}$.

Table. 2 A list of the 2-D single radar polar grid products.

Product Name	Description	Product Frequency
BREF	Base reflectivity without QC	One for each tilt
BREF_QC	Base reflectivity with QC	One for each tilt

BVEL	Base velocity without dealiasing	One for each tilt
BVEL_DA	Base velocity with dealiasing	One for each tilt
CREF	Composite reflectivity based on BREF	One per volume scan
CHGT	Height associated with CREF	One per volume scan
CREF_QC	Composite reflectivity based on BREF_QC	One per volume scan
CHGT_QC	Height associated with CREF_QC	One per volume scan
PCP_FLAG	Precipitation type (convective vs. non-convective)	One per volume scan

Table. 3 Heights of the single radar Cartesian grid levels.

Level	1	2	3	4	5	6	7	8	9	10	11
Height (km MSL)	0.5	0.75	1.0	1.25	1.5	1.75	2.0	2.25	2.5	2.75	3.0
Level	12	13	14	15	16	17	18	19	20	21	22
Height (km MSL)	3.5	4.0	4.5	5.0	5.5	6.0	6.5	7.0	7.5	8.0	8.5
Level	23	24	25	26	27	28	29	30	31		
Height (km MSL)	9.0	10.0	11.0	12.0	13.0	14.0	15.0	16.0	18.0		

The real-time test of the SRC grids for the CONUS radars was carried out using eight DELL PowerEdge 2650 machines. Each machine has two Intel Xeon 3.2GHz CPUs and 6GB of RAM. The CONUS SRC process has been running since October of 2005 and has shown to be very stable. The average CPU time for processing one volume scan of data is less than 15s and the maximum CPU time (for a wide spread precipitation) is less than 45s.

06.6.35.2 Implementation of the single radar 3-D Cartesian grids in the real-time CONUS 3D mosaic.

(This task starts in the 2nd quarter.)

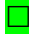


06.6.35.3 Investigate the adaptation of the new QC techniques developed for the 3D mosaic to polarimetric data fields.

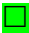
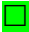
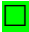
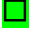

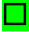




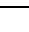
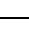
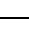
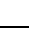
(This task starts in the 2nd quarter.)

06.6.35.4 Investigate and develop strategies for mosaicing polarimetric data fields

(This task starts in the 4th quarter.)

September FY 06
Status of Advanced Weather Radar Techniques PDT Deliverables

Legend:  Task proceeding on schedule;  Task complete;  Task incomplete and overdue.

AWRT Deliverable and Related Task	Lead Org	Due	Stat	Comment
06.6.19.1 ID useful techniques for FAA wx rdr RDAs	MITLL	30/09/06		Start 01/10/05
06.6.19.2 Collect multiple Wx scenarios for analysis	MITLL	30/09/06		Start 01/10/05
06.6.19.3 Develop framework for trade-off analysis	MITLL	30/09/06		Start 01/10/05
06.6.22.1 Coordinated studies with IFIPDT using avail. Platforms in known icing cdx	NCAR	30/09/06		Start 01/10/05
06.6.22.2 Continue analysis and verification of HCA for icing	NCAR	30/09/06		Start 01/10/05
06.6.22.3 Hi-res icing product development.	NCAR NSSL	30/09/06		Start 01/10/05
06.6.22.4 Verify HCA using WSR88DP cases	NSSL NCAR	30/09/06		Start 01/10/05
06.6.22.5 Eval. of pol. For detecting icing cdx	NSSL NCAR	30/09/06		Start 01/10/05
06.6.25.1 Polarimetric freezing level verification	NSSL	30/04/06		Start 01/10/05
06.6.25.2 Implement/test fast-track reflectivity only interim freezing level	NSSL	30/04/06		Start 01/10/05
06.6.26.1 Winter storm data collection	NSSL NCAR	30/04/06		Start 01/10/05
06.6.26.2 Winter HCA development	NSSL NCAR	30/04/06		Start 01/10/05
06.6.26.3 Winter storm particle size distribution retrieval	NCAR	30/04/06		Start 01/10/05
06.6.27.1 Archival and analysis of freezing precip data with IFI and WW PDTs	NCAR NSSL	30/04/06		Start 01/10/05
06.6.27.2 Use archived data to test NCAR HCA for freezing precip ID.	NCAR NSSL	30/04/06		Start 01/10/05

06.6.27.3 Incorporate mesoscale model output into HCA	NCAR NSSL	30/04/06	<input type="checkbox"/>	Start 01/10/05
06.6.27.4 Continue HCA development with attention to multivariate statistical techniques	NSSL NCAR	30/04/06	<input type="checkbox"/>	Start 01/10/05
06.6.27.5 Polarimetric icing hazards at multiple wavelengths	NSSL ETL	31/05/06	<input type="checkbox"/>	Start 01/10/05
06.6.29.1 Implement NTDA in ORPG	NCAR	31/04/06	<input type="checkbox"/>	Start 01/10/05
06.6.29.2 Evaluate ORDA effects on NTDA	NCAR	30/09/06	<input type="checkbox"/>	Start 01/10/05
06.6.34.1 Enhanced reflectivity QC based on NCAR REC	NSSL	31/12/05	<input checked="" type="checkbox"/>	Start 01/10/05
06.6.34.2 Develop gap-filling scheme using vertical reflectivity profiles	NSSL	30/09/05	<input type="checkbox"/>	Start 01/05/05
06.6.34.3 Verification methods for gap-filling techniques	NSSL	30/06/05	<input type="checkbox"/>	Start 01/10/05
06.6.34.4 Multi-radar synchronization	NSSL	30/09/05	<input type="checkbox"/>	Start 01/01/06
06.6.34.5 Include Canadian radar data	NSSL	30/09/06	<input type="checkbox"/>	Start 01/01/06
06.6.34.6 Create/maintain user-defined archival for CONUS 3D and 2D svr wx products	NSSL	Request-based	<input type="checkbox"/>	Start 01/10/05
06.6.35.1 Optimize single-rdr reflectivity to scalable Cartesian grid	NSSL	12/31/05	<input type="checkbox"/>	Start 01/01/06
06.6.35.2 Implement single radar 3D Cartesian grids into CONUS 3D grid	NSSL	30/09/06	<input type="checkbox"/>	Start 01/01/06
06.6.35.3 Adapt QC methods to polarimetric data	NSSL	30/06/06	<input type="checkbox"/>	Start 01/01/06
06.6.34.4 Development of polarimetric 3D mosaic.	NSSL	30/09/06	<input type="checkbox"/>	Start 01/07/06